

University of Nebraska - Lincoln

DigitalCommons@University of Nebraska - Lincoln

---

Mechanical & Materials Engineering Faculty  
Publications

Mechanical & Materials Engineering,  
Department of

---

3-23-2023

## Heterogeneous sensor data fusion for multiscale, shape agnostic flaw detection in laser powder bed fusion additive manufacturing

Benjamin Bevans

Christopher Barrett

Thomas Spears

Aniruddha Gaikwad

Alex Riensche

*See next page for additional authors*

Follow this and additional works at: <https://digitalcommons.unl.edu/mechengfacpub>



Part of the [Mechanics of Materials Commons](#), [Nanoscience and Nanotechnology Commons](#), [Other Engineering Science and Materials Commons](#), and the [Other Mechanical Engineering Commons](#)

---

This Article is brought to you for free and open access by the Mechanical & Materials Engineering, Department of at DigitalCommons@University of Nebraska - Lincoln. It has been accepted for inclusion in Mechanical & Materials Engineering Faculty Publications by an authorized administrator of DigitalCommons@University of Nebraska - Lincoln.

---

**Authors**

Benjamin Bevans, Christopher Barrett, Thomas Spears, Aniruddha Gaikwad, Alex Riensche, Harold (Scott) Halliday, and Prahalada Rao

# Heterogeneous sensor data fusion for multiscale, shape agnostic flaw detection in laser powder bed fusion additive manufacturing

Benjamin Bevans<sup>a</sup>, Christopher Barrett<sup>b</sup>, Thomas Spears<sup>b</sup>, Aniruddha Gaikwad<sup>c</sup>, Alex Riensche<sup>a</sup>, Ziyad Smoqi<sup>c</sup>, Harold (Scott) Halliday<sup>d</sup> and Prahalada Rao<sup>a</sup>

<sup>a</sup>Industrial and Systems Engineering, Virginia Polytechnical Institute, Blacksburg, VA, USA; <sup>b</sup>Open Additive, LLC, Beavercreek, OH, USA; <sup>c</sup>Mechanical and Materials Engineering, University of Nebraska-Lincoln, Lincoln, NE, USA; <sup>d</sup>Center for Advanced Manufacturing, Navajo Technical University, Crownpoint, NM, USA

## ABSTRACT

We developed and applied a novel approach for shape agnostic detection of multiscale flaws in laser powder bed fusion (LPBF) additive manufacturing using heterogeneous in-situ sensor data. Flaws in LPBF range from porosity at the micro-scale (< 100  $\mu\text{m}$ ), layer related inconsistencies at the meso-scale (100  $\mu\text{m}$  to 1 mm) and geometry-related flaws at the macroscale (> 1 mm). Existing data-driven models are primarily focused on detecting a specific type of LPBF flaw using signals from one type of sensor. Such approaches, which are trained on data from simple cuboid and cylindrical-shaped coupons, have met limited success when used for detecting multiscale flaws in complex LPBF parts. The objective of this work is to develop a heterogeneous sensor data fusion approach capable of detecting multiscale flaws across different LPBF part geometries and build conditions. Accordingly, data from an infrared camera, spatter imaging camera, and optical powder bed imaging camera were acquired across separate builds with differing part geometries and orientations (Inconel 718). Spectral graph-based process signatures were extracted from this heterogeneous thermo-optical sensor data and used as inputs to simple machine learning models. The approach detected porosity, layer-level distortion, and geometry-related flaws with statistical fidelity exceeding 93% (F-score).

## ARTICLE HISTORY

Received 16 January 2023  
Accepted 23 March 2023

## KEYWORDS

Additive manufacturing; sensor data fusion; thermal imaging; spatter monitoring; shape agnostic monitoring; porosity

## 1. Introduction



### 1.1. Goal and motivation

In the laser powder bed fusion (LPBF) additive manufacturing (AM) process, metal powder is raked or spread on a substrate (build plate), and selectively melted using energy from a laser, as shown in Figure 1 (Sames et al. 2016). LPBF is emerging as a process of choice for manufacturing high-value, geometrically complex and high-performance parts (Blakey-Milner et al. 2021). It is particularly favoured in industries, such as automotive, aerospace, energy and biomedical due to its ability to create intricate features to enhance functionality, eliminate sub-components, reduce lead time and mitigate weight (Blakey-Milner et al. 2021; Kumar et al. 2022; Sames et al. 2016).

Despite (Mostafaei et al. 2022) its demonstrated ability in reducing the time-to-market and cost, the use of LPBF parts in safety-critical industries is constrained due to the tendency of the process to generate

flaws, such as porosity and distortion in shape, and large part-to-part variation in critical features (Gordon et al. 2020; Gradl et al. 2021; Mostafaei et al. 2022; Snow, Nassar, and Reutzel 2020). Currently, LPBF parts are inspected through cumbersome and expensive non-destructive X-ray computed tomography (X-ray CT) which takes hours, if not days, for examining large parts (Blakey-Milner et al. 2021; Du Plessis et al. 2019).

To ensure the industrial-scale viability of the process and mitigate the need for extensive post-process inspection, the goal of this work is to detect multiscale flaw formation in LPBF parts as they are being printed using data from a heterogeneous in-process sensor array (Everton et al. 2016; Spears and Gold 2016). Data from multiple sensors is essential for effective process monitoring because, as shown by some representative flaws exemplified in Figure 2, flaw formation in LPBF is a result of complex, multiscale phenomena (Gordon et al. 2020; Mostafaei et al. 2022).

**CONTACT** Benjamin Bevans  benbevans@vt.edu  Industrial and Systems Engineering, Virginia Polytechnical Institute, Blacksburg, VA, USA

© 2023 The Author(s). Published by Informa UK Limited, trading as Taylor & Francis Group  
This is an Open Access article distributed under the terms of the Creative Commons Attribution License (<http://creativecommons.org/licenses/by/4.0/>), which permits unrestricted use, distribution, and reproduction in any medium, provided the original work is properly cited. The terms on which this article has been published allow the posting of the Accepted Manuscript in a repository by the author(s) or with their consent.

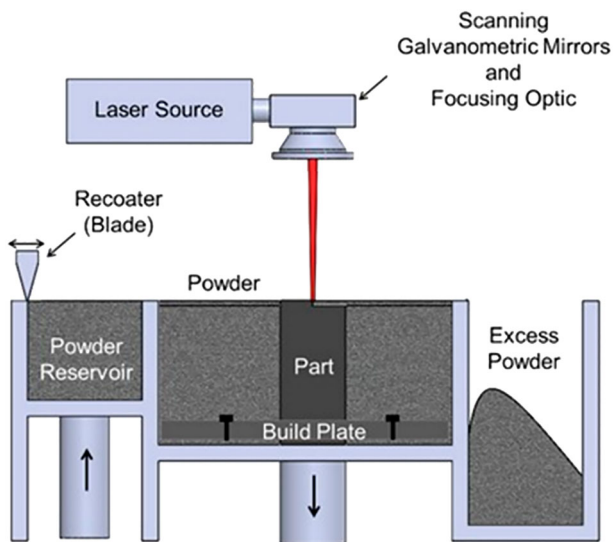


**Figure 1.** Schematic of the laser powder bed fusion (LPBF) additive manufacturing process. Metal material in the form of powder is raked, or rolled, on to a substrate (build plate) and melted layer-by-layer using energy from a laser (Gaikwad et al. 2022).

Referring to Figure 2, causal phenomena leading to flaw formation in LPBF span three length scales, ranging from the micro-scale ( $< 100 \mu\text{m}$ ), meso-scale ( $100 \mu\text{m}$  to  $1 \text{mm}$ ) and macro-scale ( $> 1 \text{mm}$ ) (DebRoy et al. 2018). At the micro-scale level the melting of the powder particles by the laser creates a pool of molten material of diameter  $\sim 100 \mu\text{m}$ , called melt pool, whose dynamics is governed by heat and mass transfer phenomena, such as Marangoni convection, Plateau-Rayleigh effect, wetting and surface tension aspects (Khairallah et al. 2016). The shape, size, temperature and spatter created by the melt pool have a causal impact on flaws, such as porosity formation, microstructure heterogeneity and mechanical properties (Chen et al. 2022; Li et al. 2022).

There are six primary mechanisms in which porosity, a primary focus of this work, is formed. These are: (i) incomplete melting of the material due to inadequate energy inputted by the laser, called lack-of-fusion porosity. Such pores are acicular and manifest a jagged irregular shape and typically exceed  $50 \mu\text{m}$  in diameter. (ii) Vaporisation of material, and gasses, dissolved in the melt pool to create gas porosity, or pinhole porosity. Such pores are circular in shape and rarely exceed  $30 \mu\text{m}$  in diameter. (iii) Excessive inputted energy by the laser that causes the laser to operate in the keyhole penetration mode. Such keyhole pores form deep within the melt pool and is roughly circular with a diameter less than  $50 \mu\text{m}$ . (iv) Ejected spatter and debris interfering with the laser melting the material and the subsequent solidification. (v) Machine-related

flaws, such as soot agglomeration on the f- $\theta$  lens of the machine affecting the amount of inputted energy. (vi) Any form of contaminants in the powder material that will interfere with the melting and solidification process of the powder (Gaikwad et al. 2022; Liu and Wen 2022; Montazeri et al. 2018; Mostafaei et al. 2022; Nassar et al. 2019; Snow, Nassar, and Reutzel 2020; Yakout et al. 2021).

Moving to the meso-scale (layer-level), the integrity of a layer is influenced by the several thousand individual laser stripes (hatches) that are fused together – in a LPBF part measuring  $1 \text{cm}^3$  there are typically 125,000 individual hatches over 625 layers (Polonsky and Pollock 2020). Improper melting of a hatch, leading to poor consolidation of a layer, will cascade across multiple layers, and is liable to cause flaws, such as layer delamination, and inter-hatch voids among others (Imani et al. 2018; Scime and Beuth 2018a).

Next, at the macro-scale part-level ( $> 1 \text{mm}$ ) the shape and orientation of the part impacts the spatiotemporal distribution of temperature within it during the process (Yavari et al. 2021b). The temperature distribution, also called the thermal history, in turn influences residual stresses, leading to deformation, which in extreme cases results in a build failure due to recoater crash or macro-cracking of the part (Kobir et al. 2022; Takezawa, Chen, and To 2021). Additionally, residual stresses generated during the build can cause distortion and cracking in parts post-removal from the substrate, thereby deleteriously effecting the geometric integrity (Yakout and Elbestawi 2020).

Further, these multiscale phenomena interact amongst each other, and are amplified by variation between machine-to-machine, resulting in flaws, such as scan path errors and lens aberrations (Gaikwad et al. 2022, 2020b; Yavari et al. 2021a). Consequently, to reliably detect flaw formation in LPBF parts it is necessary to simultaneously monitor the multiscale process phenomena ranging from the melt pool-level to the part-level. In other words, a single type of sensor may not be able to capture multiscale flaws with adequate fidelity and statistical consistency.

## 1.2. Objective, hypothesis and approach

The objective of this work is to monitor and detect multi-scale flaw formation in LPBF parts encompassing three scales: porosity, warpage, and laser scanning errors as shown in Figure 3, using data from heterogeneous sensors. The hypothesis is that flaw detection is enhanced when heterogeneous sensing modalities and subsequent analyses are matched to the scale of flaw formation. The premise being – finer scale flaws, such as porosity, require

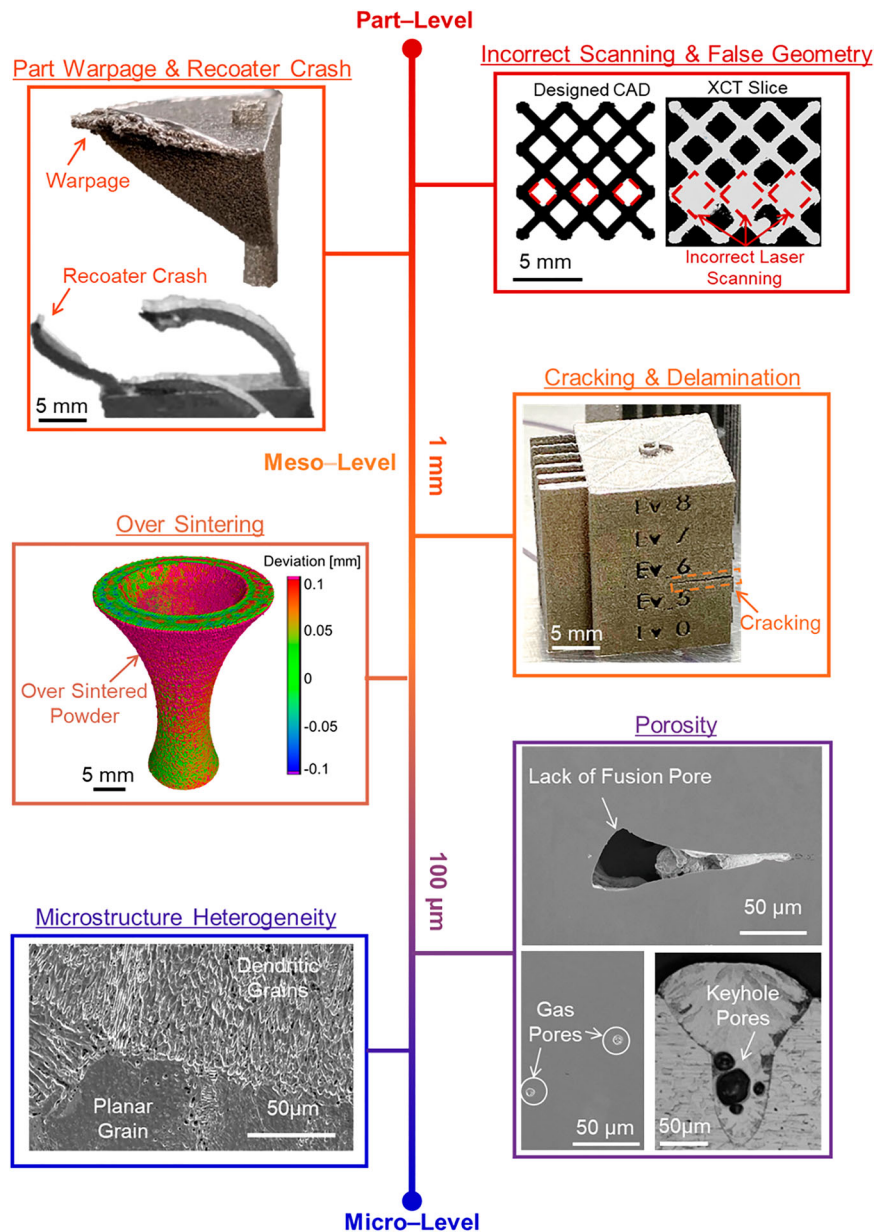


**Figure 2.** Schematic showing the multiscale nature of flaw formation in LPBF ranging from micro-scale (< 100 μm) flaws, such as porosity and microstructure heterogeneity, meso-scale cracking and layer delamination flaws, to part-level (> 1 mm) flaws, e.g. warpage and incorrect scanning.

multiple, high-resolution sensing modalities, while larger scale flaws, e.g. warpage and scanning errors, require fewer, low-resolution sensing modalities.

To realise this objective, and test the foregoing hypothesis, we installed a thermo-optical sensing array consisting of three types of sensors in an open architecture LPBF system. These three sensors are: (i) a spatter imaging camera to measure the dynamics of the melt-pool; (ii) a near infrared tomography camera with layer and hatch-level fidelity and (iii) an optical camera to image the powder bed. Shape agnostic features (process signatures) are subsequently extracted from the sensor data and used as inputs to machine learning

models trained to detect flaws that occur at multiple levels.

### 1.3. Prior work and novelty

Recent review articles provide insights into approaches for in-process sensing and monitoring in LPBF (Everton et al. 2016; Grasso et al. 2021; Grasso and Colosimo 2017; Mani et al. 2017; Spears and Gold 2016). A concurrent research thrust area is in the analysis of the large amount of data acquired by in-process sensors, and the subsequent correlation of the signatures extracted from the sensor data to specific flaws using machine

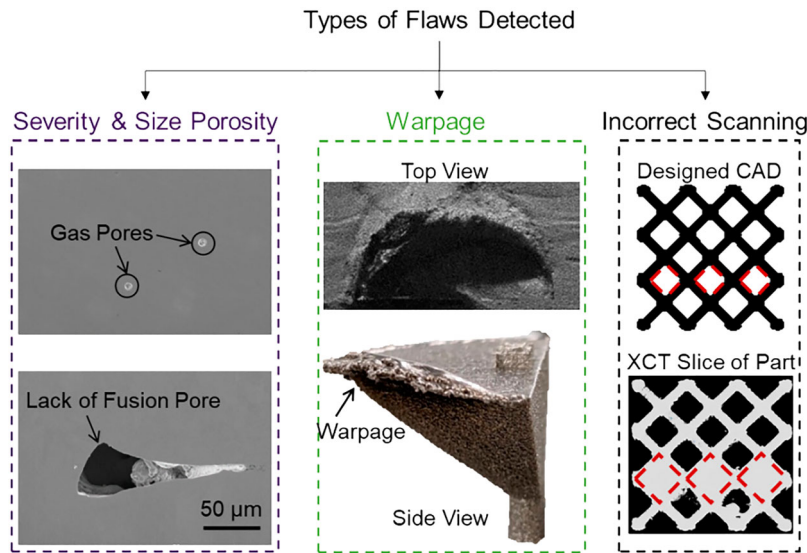


**Figure 3.** Three types of flaws were observed and studied in this work: micro-scale porosity, layer-level warpage and part-level scan errors.

learning techniques (Jin et al. 2020; Mahmoud et al. 2021; Meng et al. 2020; Wang et al. 2020). Representative literature concerning the type of sensors used, signatures (features) extracted, data analytics approach developed and the type of flaw detected are summarised in Table 1.

Gaikwad et al. (2022) monitored the meltpool using a system of coaxial high-speed cameras. They

subsequently extracted physically intuitive shape, spatter and temperature distribution characteristics of the meltpool and correlated these sensor signatures to the type and severity of pore formation. They used simple machine learning approaches, such as k-nearest neighbours (KNN) and support vector machine (SVM) to make these signature-porosity correlations. They further compared the prediction fidelity of such simple

**Table 1.** Summary of literature comparing various sensing modalities, signal analysis algorithms and various types of flaws. K-nearest neighbours (KNN), support vector machine (SVM), neural network (NN), convolutional neural network (CNN), gaussian mixture modelling (GMM), Decision Tree (CART), Random Forest (RF), XGBoost(XGB), Generative Adversarial Network (GAN).

Ref	Sensor Used	Signatures Extracted	Analytics Methods	Detected Flaws	Flaw Level
Gaikwad et al. (2022)	Two high-speed cameras	Meltpool shapes & temperature distribution	KNN, SVM, CNN	Porosity type and lensing artefacts	Micro-scale
Smoqi et al. (2022)	Imaging pyrometer	Meltpool shape & temperature distribution	KNN, SVM	Porosity	Micro-scale
Petrich et al. (2021)	Electro-optical, acoustic emissions	Raw images, hatch angle, contour distance	Shallow NN	Porosity	Micro-scale
Scime and Beuth (2019)	High-speed camera	Meltpool gradient	SVM, NN	Meltpool stability	Micro-scale
Nguyen et al. (2023)	Optical camera	Raw images of powder bed	Deep NN	Porosity, overheating, & warpage	Micro- & Meso-level
Scime and Beuth (2018b)	Optical camera	Raw images of powder bed	CNN	Recoater effects, warpage, & debris	Meso-scale
Xiao, Lu, and Huang (2020)	Optical camera	Raw images of powder bed	CNN, SVM	Warpage, part shifting, short feed	Meso-scale
Land et al. (2015)	Three optical cameras & a digital projector	Image projection phase & intensity	Topography Analysis	Distortion in powder bed	Meso-scale
Pandiyani et al. (2021)	Acoustic sensor	Raw signal	GAN	Anomalies	Meso-scale
Li et al. (2018)	Two cameras & projector	Layer height map	Topography Analysis	Deviation in powder bed & contour deviation	Meso- & Part-level
Okaro et al. (2019)	Two photodiodes	Signal Basis	GMM	Poor tensile strength.	Part-level
Huang and Li (2021)	Pressure sensors & thermocouples	Chamber and build environment status	CART, RF, XGB	Poor yield & tensile strength	Part-level
Gaikwad et al. (2019)	Optical camera	Raw images of powder bed	CNN	Geometric integrity	Part-level

machine learning techniques to complex black-box deep machine learning algorithms. Gaikwad et al. (2022) reported that a set of physically intuitive process signatures, when combined with simple machine learning models, were found to outperform complex deep learning models that directly used the sensor data without decomposing the sensor signals into process signatures. Similar results affirming the effectiveness of leveraging low-level, yet physically interpretable, process signatures with simple machine learning models are evident in recent works by other researchers (Gaikwad et al. 2020a; Smoqi et al. 2022).

Huang and Li (2021) used global monitoring statistics, such as: build chamber temperature and pressure, powder flowability and part geometry features to predict percentage elongation, yield and tensile strength via simple supervised regression machine learning models. No active melt pool or part level monitoring was performed in their work.

Petrich et al. (2021) used a sensor fusion approach combining in-situ electro-optical images, acoustic and multi-spectral emissions sensing to determine the severity of porosity in the samples. Petrich et al. (2021) organised the data into a 3D voxel space and correlated the raw data in those voxels to porosity found using neural networks.

Pandiyan et al. (2021) used an acoustic sensor to continuously collect data at 1 MHz. This data set was then used to train semi-supervised machine learning models, specifically a generative adversarial network (GAN), to detect if a layer was free of any form of anomaly (flaw). The authors' approach detected the presence of a flaw in a part with a fidelity of ~96%, however, the specific flaw generated could not be discerned from the developed models.

Scime and Beuth (2018b) used raw images acquired after recoating of a layer to detect varying types of recoater effects, warpage and debris on the powder bed using a deep learning convolutional neural network. Similarly, Li et al. (2018), used two optical cameras and fringe projection to perform topography analysis. This provides a height map of the powder bed after recoating, allowing for the detection of warpage and recoater effects.

Nguyen et al. (2023) also used an optical layer wise imaging camera to detect the presence of flaw formation. In this work, Matlab-generated deep learning neural networks were trained to monitor the surface morphology of each part, after the deposition of a layer, to detect the existence of lack-of-fusion porosity, overheating and warpage.

The following two gaps in the current literature are revealed from this review.

- (1) Most data-driven models have been demonstrated in the context of one type of part shape, typically a simple cube or cylinder (Imani et al. 2018; Montazeri et al. 2020; Smoqi et al. 2022). Moreover, the data originates from one build plate. Approaches that use data from different builds, with varying part shapes made under different locations and orientations remains to be demonstrated. In other words, the scalability and transferability of the approach across different part shapes, orientations and over multiple builds is yet to be ascertained (Mahmoud et al. 2021).
- (2) Machine learning models have been trained to detect one type of flaw, such as porosity or distortion, based on input data from one type of sensor. Detection of multiple different types of flaws based on data acquired from a heterogeneous sensing array remains an open challenge (Grasso et al. 2021; Mani et al. 2017).

This work addresses the foregoing gaps – it uses multiple heterogeneous sensors to detect multiscale flaws in different part geometries, and further, validates the approach across different build plates, part locations and orientations. Indeed, it is one of the first works that detects three types of trans-scale flaws based on data from three different types of sensors: porosity, recoater crash and geometric variation due to scanning errors.

The rest of this paper is organised as follows. In Section 2 we describe the setup, sensing system and experiments conducted. Section 3 details the signal analysis and machine learning approach used for monitoring of multiscale flaws. Section 4, details the results and the statistical fidelity of the devised approach in detecting multiscale flaws. Finally, conclusions are summarised in Section 5.

## 2. Experiments

### 2.1. Apparatus and sensing setup

Parts were manufactured on the PANDA LPBF machine by Open Additive. This system allows an operator the freedom to change processing parameters between layers of the same part and between parts on the same build plate. In-process data was acquired using Open Additive's proprietary AMSENSE™ sensor suite which includes three thermo-optical imaging sensors. Schematic of the sensing system are shown in Figure 4, and manufacturer set sensor specifications are summarised in Table 2 (O. Additive 2021).

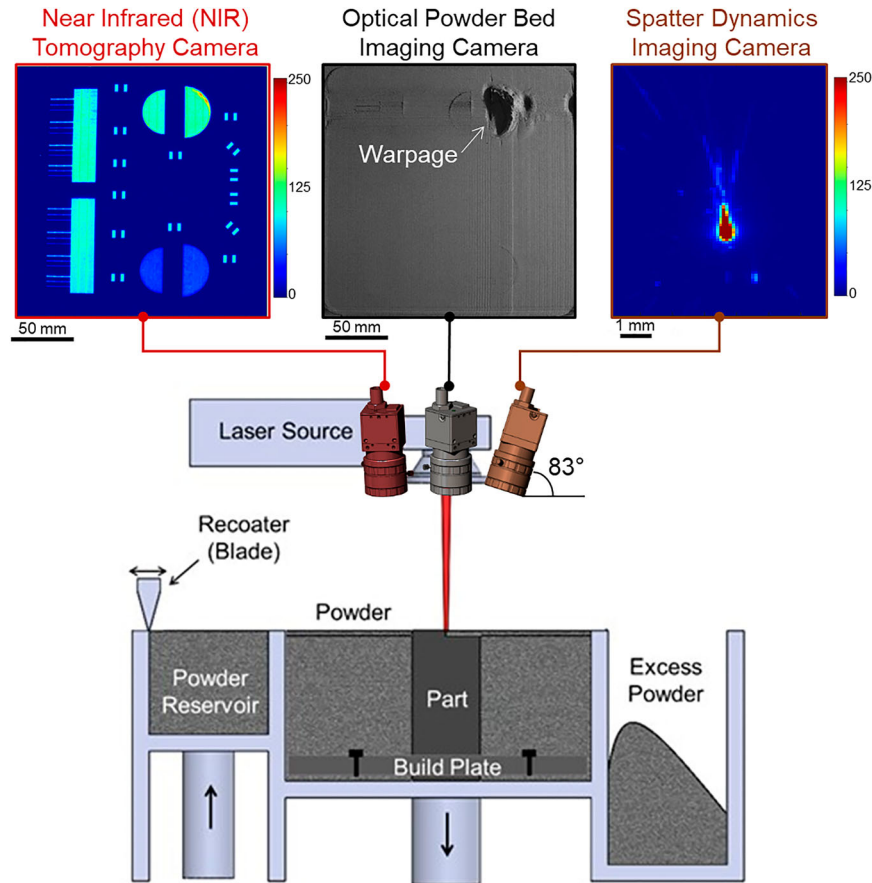


**Figure 4.** Schematic of the sensor location and orientation in the Panda Open Additive LPBF machine. Three types of sensors are installed on an optical table on top of the machine near the laser source: a near-infrared thermal imaging camera, a powder bed imaging camera and a high-speed meltpool spatter dynamics imaging camera.

The three sensors were installed and calibrated by the manufacturer (Open Additive) on an optical table on the top of the LPBF machine and are on an off-axis (staring) configuration inclined at  $83^\circ$  to the build plate. The entire build plate is captured within the field-of-view of the sensor array. The sensing system is designed with the intent to observe multiple phenomena across different length scales. The three sensors are as follows: (1) a near infrared (NIR) thermal imaging camera with wavelengths of 700–1000 nm, also referred to as a tomography sensor; (2) a high-speed imaging

camera to capture meltpool spatter; and (3) an optical powder bed imaging camera.

Example data from the sensing system are shown in Figure 4. The NIR camera observes the layer-level surface temperature distribution. To explain further, the NIR thermal imaging camera is set with a long 250 ms exposure time, sampling at four frames per second, and is used to capture the thermal intensity of the meltpool upon laser strike. The thermal intensity of the meltpool is subsequently consolidated for an entire layer to estimate the layer-level part surface temperature.

**Table 2.** Specifications of the three sensors used in these experiments: NIR Tomography, optical powder bed imaging and high-speed spatter imaging.

Type of Sensor	Phenomena Measured	Make and Model	Sampling Rate	Resolution
Optical Powder Bed Imaging	Meso-scale recoater and layer-level flaws.	Basler acA4024-29um	2 images/layer post lasing & recoat	12 megapixels
Near Infrared Tomography (NIR)	Intensity at the instance of laser strike.	Basler acA4024-29um with NIR filter	4 Frames per Second 250 millisecond exposure	12 megapixels
High-Speed Spatter Dynamics Imaging	Meltpool dynamics.	Basler acA1920-155um	150 frames per second 500 $\mu$ s exposure	2.3 megapixels



With the meltpool spatter imaging camera, images of the meltpool were captured with a relatively high sampling rate of 150 frames per second. This camera thus observes the micro-scale meltpool-level phenomena, specifically the spatter dynamics. The lowest resolution sensor is the optical imaging (recoater) camera which captures two images per layer, one post-recoat and one post-sintering. In this work, only the post-recoat images from the recoater camera were analysed to visualise flaws associated with the recoating process.

## 2.2. Build plate and part geometry

Three build plates were manufactured to test the effectiveness of the approach across multiple processing conditions. Each build plate has four different part shapes (geometries) for a total of 22 parts per build plate – thus there are a total of 66 parts. The powder material for the build is Nickel Alloy 718 (Inconel 718, UNS N07718) and has a mean and standard deviation particle size of 45 and 15  $\mu\text{m}$ , respectively. Nickel Alloy 718 is favoured by the aerospace engine industry for its high-temperature properties (Sanchez et al. 2021). The build plate (low carbon steel) measures 152 mm  $\times$  152 mm  $\times$  25 mm (thick). The builds were conducted in a Nitrogen environment.

The build plate layout and geometries for a representative case are shown in Figure 5. The four types of geometries are: (i) overhang geometries ( $\times 14$ ); (ii) cones ( $\times 4$ ); (iii) lattice-shapes ( $\times 2$ ) and (iv) thin-wall structures ( $\times 2$ ). This work does not analyse data from the thin-wall parts owing to the difficulty in obtaining the X-ray computed tomography (X-ray CT) characterisation of these parts due to their large volume. The build consists of 733 layers and required  $\sim 18$  h to complete.

Parts were manufactured under different process conditions. Eleven parts near the top half of each build plate, closer to the gas flow as shown in Figure 5, were manufactured under fixed processing parameters. These parameters were determined based on extensive *a priori* optimisation studies. Fixed processing implies that all processing parameters, such as laser power and velocity, reported in Table 3, remain constant throughout the build. The bottom half of the build plate (Figure 5), farther from the gas flow (11 parts), is a mirror image of the top half. The parts farther from the gas flow were processed under dynamic processing conditions by varying the laser power between layers. The aim of dynamic processing was to deliberately

induce flaw formation. The processing conditions are summarised in Figure 6, and discussed herewith.

### (a) Overhang

As shown in Figure 5, 14 total overhang geometries are created on each build plate. These parts are 22 mm tall and consist of 733 layers (Figure 6). These overhang geometries are built with variation in processing parameters, shape, location on the build plate, and orientation with respect to the recoater direction.

Seven overhang parts located at the top of the build plate were manufactured with fixed (nominal) processing parameters that remained constant throughout the overhang section of the geometry (laser power). These nominal processing parameters are reported in Table 3.

The nominal processing parameters used in this work are the default settings for a specific material that are provided to the user by the machine manufacturer (Open Additive). These parameters for Nickel Alloy 718 were obtained via an extensive parameter study which involved building cuboid shapes under various laser power, velocity, hatch spacing, layer height, gas flow conditions, among others. The parameters that result in a maximally dense part with no detectable porosity were chosen. The efficacy of these parameter settings is also verified in the current work via the parameter study in this work in reference to the overhang parts (see Figure 6).

The key nominal processing parameters provided by the manufacturer are: laser power  $P = 230$  W, velocity  $V = 1200$  mm $\cdot$ s $^{-1}$ , hatch spacing  $h = 70$   $\mu\text{m}$  and layer height  $H = 30$   $\mu\text{m}$ . These processing parameters result in a volumetric energy density,  $E_v = P/(V \times H \times T) = 91$  J $\cdot$ mm $^{-3}$ .

Furthermore, in Figure 5(a), the cuboid-shaped base of the fixed overhang geometries located on the top of the build plate (fixed parameters), were processed under varying laser power conditions to study the effect of processing parameters and to validate the manufacturer's recommended nominal processing parameters. These laser power conditions are summarised in Figure 6.

The seven overhang parts located at the bottom of the build plate, farther from the gas flow, were made under processing parameters that were varied during the build, specifically in the overhang section of the geometry. As summarised in Figure 6, these overhang parts built under varying laser power setting are termed dynamic processing. The overhang angle ( $\theta$ ) was also varied at three levels from  $\theta = 50^\circ$ ,  $45^\circ$  and

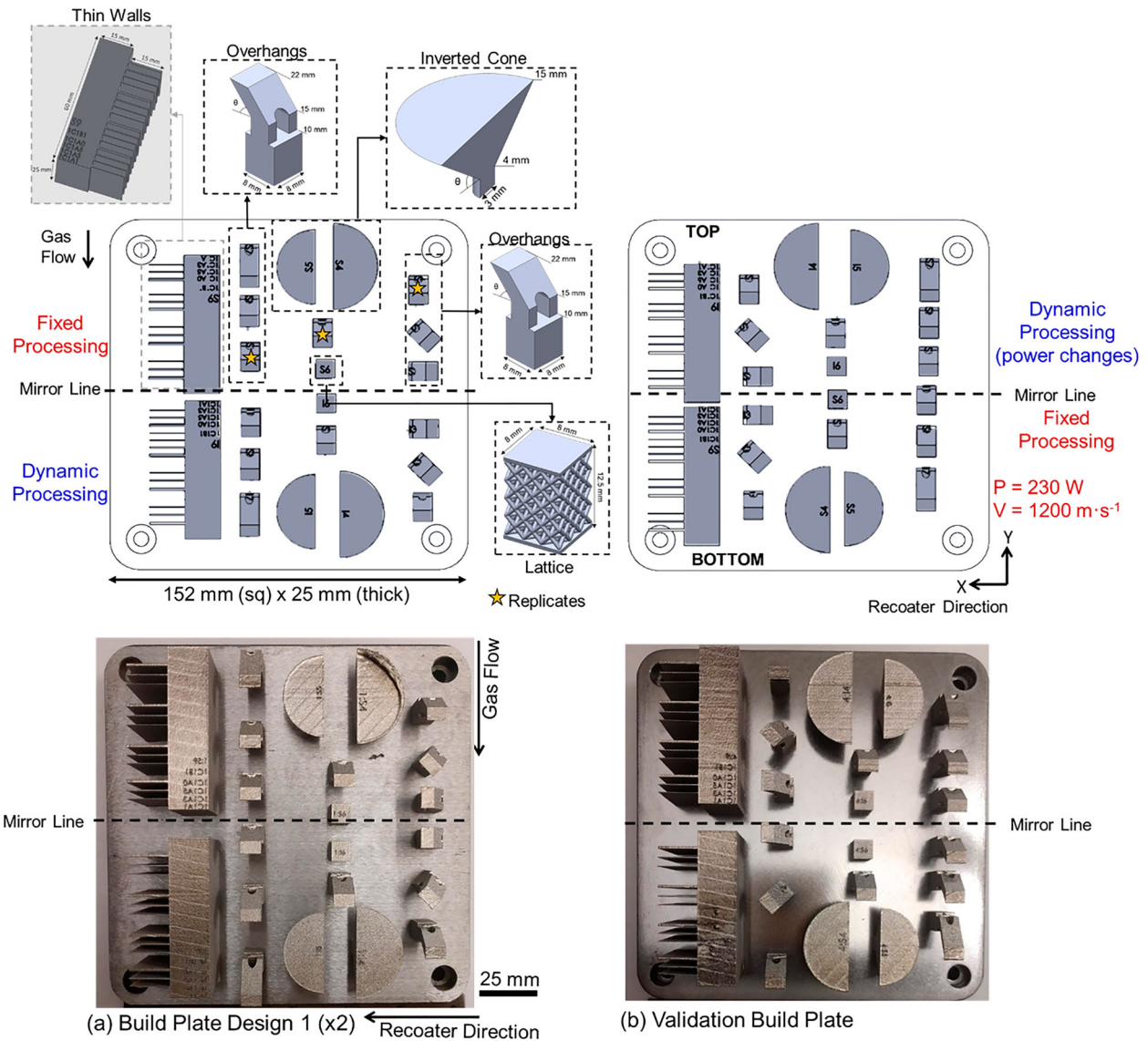


**Figure 5.** Build layout and dimensions of printed parts across two build plate designs. The build plate design shown in (a) is repeated twice; there are total of three build plates. A total of 22 parts are processed per build plate. These 22 parts encompass variation in geometry, location and processing parameters to ensure shape agnosticism. For the build plate shown in (a) parts made under fixed laser power condition of  $P = 230\text{ W}$  are located on the top half of the build plate. Parts on the bottom half, farther from the gas flow vents are built with varying processing parameters, called dynamic processing. The build plate in (b) is a mirror image ( $180^\circ$  rotation) of (a), it is called the validation build plate and has identical parts, but different layout and processing condition.

$30^\circ$ . Six of the fourteen parts with  $\theta = 50^\circ$  are located nearer to the recoater start position on the right-hand side of the build plate. Next, to account for the effects of orientation of the part relative recoater blade, the angle of rotation ( $\alpha$ ) of these parts, with reference to the direction of the recoater blade, is varied from  $\alpha = 0^\circ, 45^\circ$  and  $90^\circ$ .

Three replicate overhang geometries with  $\theta = 50^\circ$ ,  $\alpha = 0^\circ$  and  $P = 230\text{ W}$  were printed on both sides of the build plate, demarcated with a yellow star in Figure 5.

(b) Cone

Four cone geometries were created per build plate. Each cone geometry is 15 mm in height and contains 500 layers. The cone parts were built with varying inclination angles ( $\theta = 35^\circ, 40^\circ$ ) and processing conditions. These severe inclination angles are liable to cause deformation and recoater crashes (Diegel, Nordin, and Motte 2019; Kobir et al. 2022). Hence, a soft rubber recoater material was used to avoid stopping the build due to part distortion-induced recoater crashes.

Two cones were placed near to the gas flow at the top of the build plate, built under fixed processing parameters, and two cones are located on the far side of

**Table 3.** Nominal parameters used in the Open Additive PANDA LPBF machine.

Process Parameter [Units]	Values
Laser type and wavelength.	Ytterbium fibre, wavelength 1070 nm continuous mode, 500 W max power
Nominal Laser Power ( $P_0$ ) [W]	230
Scanning Speed (V) [ $\text{mm}\cdot\text{s}^{-1}$ ]	1200
Hatch spacing (H) [mm]	0.07
Layer thickness (T) [mm]	0.03
Volumetric global energy density $E_v$ [ $\text{W}/\text{mm}^3$ ]	91
Laser spot size [ $\mu\text{m}$ ]	50
Scanning strategy	Meander-type scanning strategy with 66-degree rotation of scan path between layers.
Build atmosphere	Argon
Powder Material Properties	
Material type	Nickel Alloy 718 (Inconel 718); corresponding to UNS N07718 (sourced from Praxair)
Particle size range [ $\mu\text{m}$ ]	15–45 (D10 – D90)

the gas flow under dynamic processing parameters, i.e. the laser power was changed layer-by-layer, as detailed in Figure 6.

#### (c) Lattice

Two lattice structures were processed per build plate. Lattices are complex, intricate geometries that are apt candidates for LPBF, but often fail due to scanning errors (Ibrahim et al. 2020). The lattice geometry is based on a body-centred cubic structure and repeats four times in the Z direction (build height). Each lattice is 12.5 mm in height and consists of 416 layers. As detailed in Figure 6, one lattice shape was produced under fixed processing parameters and the other lattice was produced under dynamic processing conditions, with laser power changes.

### 2.3. Validation build plate

To validate the transferability, and shape and location agnostic characteristics of the approach, a third build plate was manufactured (Figure 5(b)). The intent is to quantify the Type I (false positive), and Type II (false negative) error rates of the approach. The validation build plate contains identical parts as the two build plates described before in Section 2.2, however, the locations of the samples were rotated by 180°. In the context of Figure 5(b), in the validation build plate parts produced under fixed processing parameters were located farther from the gas flow, and the dynamic-processed parts are at the top of the build plate near the gas inlet.

Further, to rigorously test the fidelity of the detection algorithm given changes in the process conditions, the two dynamic-processed cones had a different laser power change from layer-to-layer. The laser power was maintained at a nominal level of 230 W up to 8 mm (layer 267) build height and then reduced to 160 W to prevent the warpage found in the fixed cone geometries. The rest of the samples on the validation build plate are identical with respect to their processing parameters as summarised in Figures 5 and 6.

### 2.4. Post-process characterisation

The 14 overhang geometries, 4 cones, and 2 lattice structures were examined with X-ray computed tomography (X-ray CT). The overhang and lattice geometries were scanned at a resolution of 15  $\mu\text{m}$  per voxel while the inverted cone geometries were scanned at 25  $\mu\text{m}$  per voxel (NorthStar Imaging Model X3000). The lower scan resolution for the inverted cone geometry is due to the relatively larger size of the sample.

Porosity is characterised as: (i) pore severity in terms of percent volume porosity per layer, called defect volume ratio (DVR); and (ii) pore size (diameter) in micro-meters ( $\mu\text{m}$ ). These measurements were obtained using Volume Graphics software native to the X-ray CT machine.

To characterise porosity type and size the cone-shaped parts were examined with optical microscopy. For this purpose, the parts were cross-sectioned using electro-discharge machine and polished to Ra  $\sim$  50 nm surface finish in progressive steps using an alumina abrasive-based slurry.

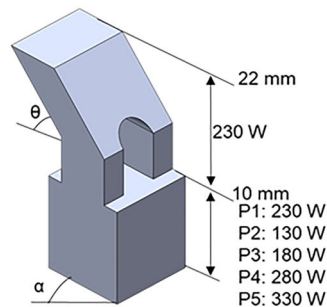
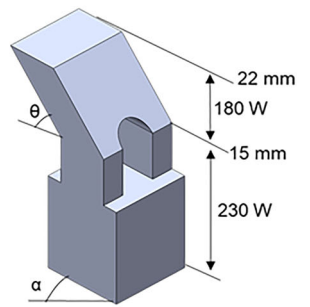
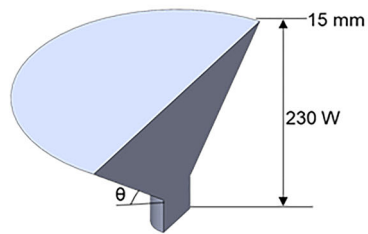
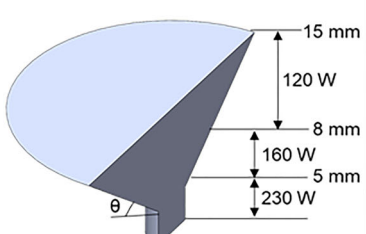
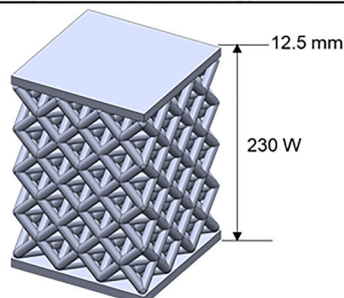
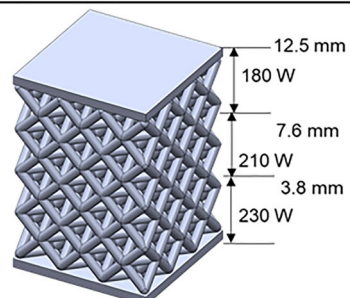
## 3. Signal analysis, data fusion and machine learning

### 3.1. Overview

As summarised in Figure 7, the objective of this work is to detect multiscale flaw formation in LPBF by combining (fusing) data from the three thermo-optical sensors within simple machine learning models. In this work, flaw detection is performed on a layer-by-layer basis; this includes the porosity, warpage and geometric integrity flaw detection.

There are three machine learning tasks. Task 1: (A) detect severity and (B) size of porosity; Task 2: detect part deformation (warpage) and Task 3: detect geometry-level flaws resulting from laser scanning errors. Each of these tasks requires the following three steps described in depth in the following sections:

(Step 1) – Data Consolidation: Representing temporal images into a layer-wise form.

Fixed Processing	Dynamic Processing
<p><b>Overhangs:</b> Vary process parameters, shape, location, and orientation. 7 parts were made under both fixed and dynamic processing conditions.</p>	
 <p style="text-align: center;">Inclination: <math>\theta = 30^\circ, 45^\circ, \text{ and } 50^\circ</math> Rotation: <math>\alpha = 0^\circ, 45^\circ, \text{ and } 90^\circ</math></p>	 <p style="text-align: center;">Inclination: <math>\theta = 30^\circ, 45^\circ, \text{ and } 50^\circ</math> Rotation: <math>\alpha = 0^\circ, 45^\circ, \text{ and } 90^\circ</math></p>
<p><b>Cone:</b> Vary process parameters and shape. 2 inverted cones at each processing condition one at <math>\theta = 35^\circ</math> and <math>40^\circ</math></p>	
 <p style="text-align: center;">Inclination: <math>\theta = 35^\circ \text{ and } 40^\circ</math></p>	 <p style="text-align: center;">Inclination: <math>\theta = 35^\circ \text{ and } 40^\circ</math></p>
<p><b>Lattice:</b> Vary process parameters. 1 lattice at each processing condition.</p>	
	

**Figure 6.** Processing plan for each geometry of interest and purpose for changes. The fixed overhang geometries contained a parameter cube experiment in the base to validate processing parameters. However, all other geometries printed under fixed processing parameters used the nominal processing condition.

- (Step 2) – Dimension Reduction and Feature Extraction: Deriving low level spectral signatures from each layer-wise-image.
- (Step 3) – Data Fusion: Synthesising data across layers and different sensors.

**3.2. Step 1 – data consolidation**

In this step temporal data for a particular layer from each sensor is consolidated as a 2D image of a layer. For each

geometry a single image of the powder bed imaging, NIR tomography and spatter cameras were extracted for every layer. Sample data for layer 400 is shown in [Figure 7](#).

For example, the NIR tomography camera in [Figure 7](#) (a2) depicts uneven heat distribution on the edges of the cone, indicating the causal thermal phenomena that lead to warpage and distortion. Likewise, an individual frame of the meltpool captured by the spatter imaging camera is shown in [Figure 7](#)(c1). Consolidating all such

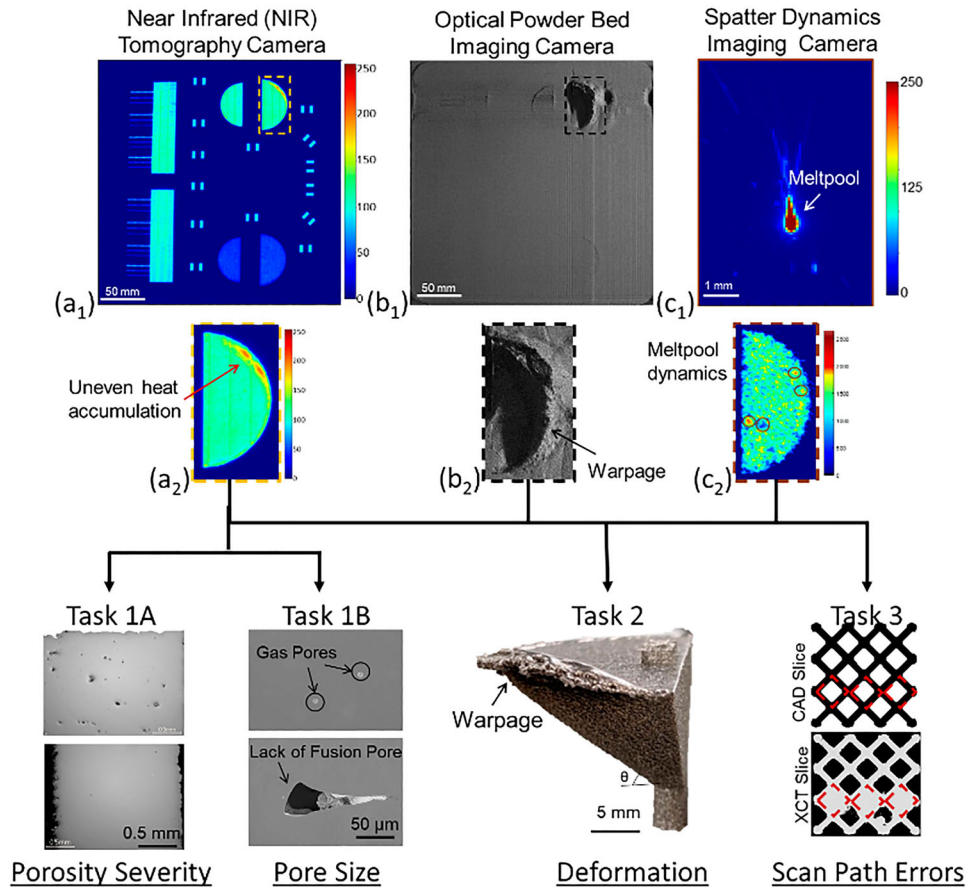


**Figure 7.** Output from each type of sensor for layer 400 of the cone shaped part with  $\theta = 35^\circ$  when warpage is observed. (a1–c1) are the raw data acquired from layer 400, (a2–c2) is data acquired for the region of interest.

frames for a layer results in the relative spatter intensity image shown in Figure 7(c2). Visual observation of the meltpool spatter pattern captured by the spatter camera in Figure 7(c2) reveals the presence of extreme spatter events. Simultaneously the NIR tomography camera detects uneven heat distribution.

### 3.3. Step 2 – dimension reduction and feature extraction

In the feature extraction step, depicted in Figure 9, the layer-by-layer data from each type of sensor image consolidated in Step 1, is quantified in terms of a single feature called the graph Laplacian spectral radius ( $\lambda_N$ ) (Shi 2007). The spectral radius ( $\lambda_N$ ) ranges between 1 and 2 and thus provides a means to reduce the high dimensional information contained in an image to a single number (Chung 1997).

The spectral radius is obtained in three phases. First in phase 1, visualised in Figure 8, a layer image from each type of sensor is discretised into  $m \times n$  pixel grids, herein  $m = 15$ ,  $n = 10$ , resulting in a  $15 \times 10$  matrix. The rows of this so-called patch matrix  $\mathbf{P}$  are

subsequently reshaped to obtain a column vector  $\bar{p}$  of size  $150 \times 1$ .

We note that each imaging sensor has a different spatial and temporal resolution. Hence, the size of the patch matrix  $\mathbf{P}$  must be calibrated to the resolution of each sensor. This was done through extensive offline optimisation not discussed in this paper. The recoater camera had a patch size of  $30 \times 20$  pixels, for the tomography and spatter images the patch size was ideal at  $3 \times 5$  pixels. This finer scale for the tomography and spatter images is due to these sensors observing the finer scale meltpool and temperature dynamics. In contrast, the recoater camera only observes warpage and other powder bed flaws at a relatively low resolution.

Next in phase 2, an adjacency matrix  $\mathbf{W} = [w_{ij}]$  is created from the patch vector  $\bar{p}$  using the following relationship.

$$w_{ij} = \bar{p}_i - \bar{p}_j^2 \quad (1)$$

Where  $\bar{p}_i$  is the  $i$ th patch vector originating from the  $i$ th patch matrix  $\mathbf{P}_i$  in the patch-by-patch image. In other words, the patch matrix is an area-wise restructuring of the raw image in matrix form, that is then

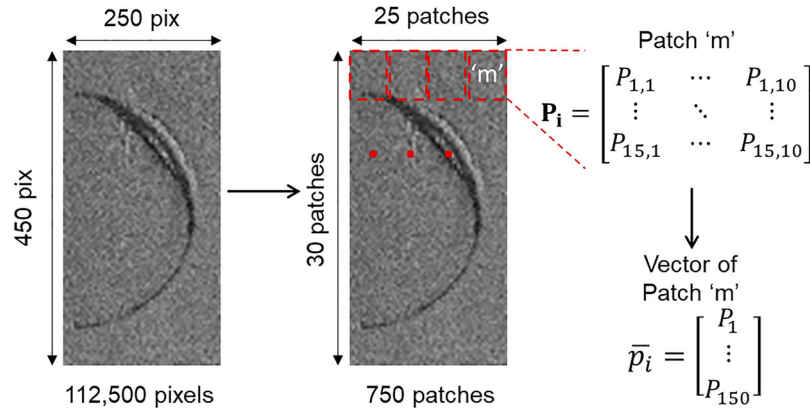


**Figure 8.** Vectorised each patch in an image in order to cluster multiple pixels together. The adjacency matrix is obtained by calculating the Euclidean distance from one patch to another patch.

converted into a vector to calculate the adjacency matrix  $\mathbf{W}$ . The element  $w_{ij}$  of the adjacency matrix  $\mathbf{W}$  is the Euclidean distance ( $L_2$  norm) between the  $i$ th and  $j$ th patch vector in the image. Thus, a relative relationship is established between the pixel intensity of one patch to every other patch in the image. The size of the patch matrix  $\mathbf{P}_i$  influences the computational time. As the size of the patch matrix decreases the resolution of the resulting adjacency matrix  $\mathbf{W}$  increases at the expense of computation time.

In phase 3, the diagonal degree matrix  $\mathbf{D}$  is derived from the adjacency matrix as follows:

$$d_i = \sum_{j=1}^{j=N} w_{ij} \quad (2)$$

Subsequently, the weighted Laplacian matrix ( $\mathcal{L}$ ) is calculated using the following equation:

$$\mathcal{L} = \mathbf{D} - \mathbf{W} \quad (3)$$

The eigenvalues ( $\lambda$ ) and eigenvectors ( $v$ ) of each layer-wise consolidated image data can then be extracted from the Laplacian matrix:

$$\mathcal{L}v = \lambda v \quad (4)$$

The largest eigenvalue, called the spectral radius ( $\lambda_N$ ), is selected as the monitoring statistic (Chung 1997). The result of phase 3 is visualised in Figure 9. The rationale for using the Laplacian eigenvalues as a monitoring statistic has been studied extensively in our previous work (Montazeri and Rao 2018; Tootooni et al. 2018). The spectral radius captures the degree of inhomogeneity in an image. The more inhomogeneous an image, the closer the value of  $\lambda_N$  is to 1. Conversely, the more homogenous an image,  $\lambda_N$  approaches 2. Moreover, the spectral radius is independent of image scale and size (Shi 2007).

### 3.4. Step 3 – incorporation of process history and layer-by-layer data fusion

A drawback of the spectral radius ( $\lambda_N$ ) statistic is that it does not incorporate layer-by-layer evolution of the process – each layer is treated independent of the preceding and subsequent layers. For example, previous research in the literature affirms a correlation of melt-pool behaviour across layers (Ulbricht et al. 2021). To account for this temporal dependency, the spectral radius from the NIR tomography ( $\lambda_{N,T}$ ), spatter ( $\lambda_{N,S}$ ) and recoater ( $\lambda_{N,R}$ ) cameras are further processed through an exponentially weighted moving average (EWMA) filter (Ramirez and Ramirez 2018). The filter is mathematically expressed as follows:

$$\Lambda_L = \varepsilon \lambda_N^L + (1 - \varepsilon) \Lambda_{L-1} \quad (5)$$

Where  $\lambda_N^L$  is the spectral radius at layer  $L$ . This recursive function applies a weight ( $\varepsilon$ ) to the spectral radius obtained from the previous layers. Using a weight of  $\varepsilon = 0.1$ , implies that the previous four layers are weighted at 65%, which corresponds to melt-pool penetration depths of 2–4 layers typically observed in LPBF (Schwerz and Nyborg 2021).

The result of applying this exponentially weighted moving average filter from all three sensors for the cone geometry, that showed severe warpage (see Figure 5), is presented in Figure 10. The function  $\Lambda_L$  for the tomography ( $\Lambda_L^T$ ) and spatter ( $\Lambda_L^S$ ) sensors show a prominent decreasing trend which correlates to the warpage in the sample. This is because, as heat begins to accumulate on the edges and the melt-pool becomes unstable, the layer-wise image data becomes less homogeneous. This leads to a decrease in connectivity in the graph-based representation of the image, and consequently, a decrease in  $\lambda_N$ .

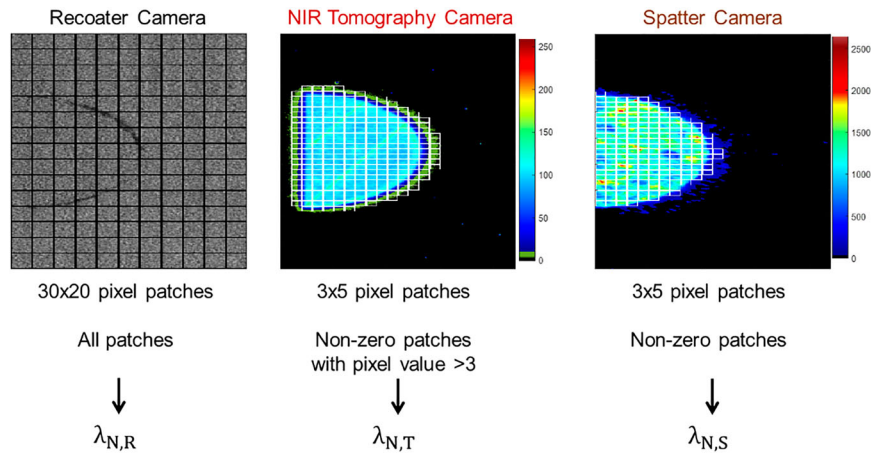


**Figure 9.** The spectral radius ( $\lambda_N$ ) is extracted for each layer of data obtained from each sensor. Depending on the sensor, different patch size & criteria were chosen.

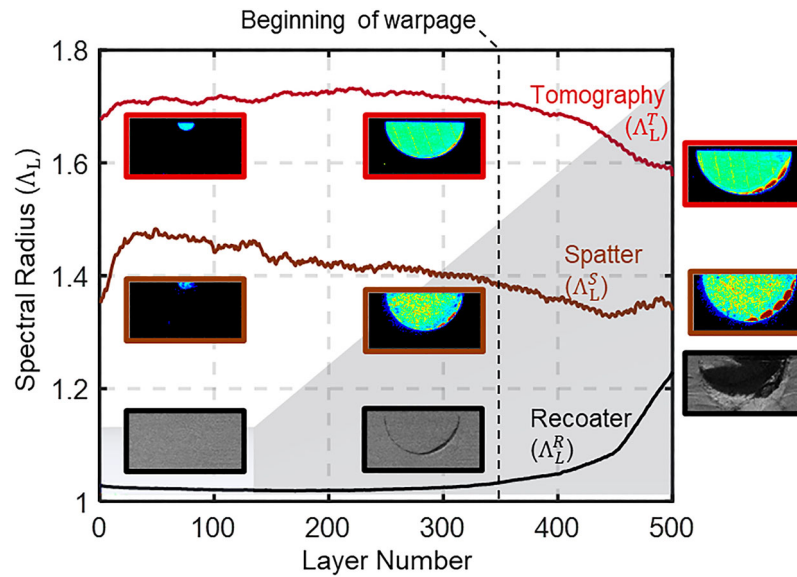


**Figure 10.** Behaviour of spectral radius as a function of layers for warpage flaws. Warpage is observed after layer 350. There is a sharp change in the spectral radius for various sensors due to the onset of warpage.

However, the  $\Lambda_L$  for the recoater camera ( $\Lambda_L^R$ ) increases with incipient warpage. This is caused because, unlike the tomography and spatter cameras, the natural state (nominal condition) of the recoater image data is inhomogeneous, leading to a low spectral radius number. The image data collected for the raw powder bed (no warpage state) has relatively extreme variation in pixel values that lead to this inhomogeneity. When the sample begins to warp above the powder bed, the image becomes homogeneously dark. Thus, the spectral radius number for the powder bed optical imaging (recoater) sensor increases in value when the sample begins to warp.

### 3.5. Machine learning – model training, testing and validation

#### 3.5.1. Model structure

Figure 11 summarises the approach in terms of process signatures and detection algorithms used in this work. The aim of machine learning is to determine multiscale flaw formation at the porosity-, warpage- and geometry-levels. For this purpose, a total of four features were extracted. The three EWMA-filtered spectral radii from the recoater ( $\Lambda_L^R$ ), NIR tomography ( $\Lambda_L^T$ ) and spatter ( $\Lambda_L^S$ ) sensors, and the mean meltpool intensity ( $I_L$ ) for each layer ( $L$ ) extracted from the NIR tomography camera. Meltpool intensity was found to be

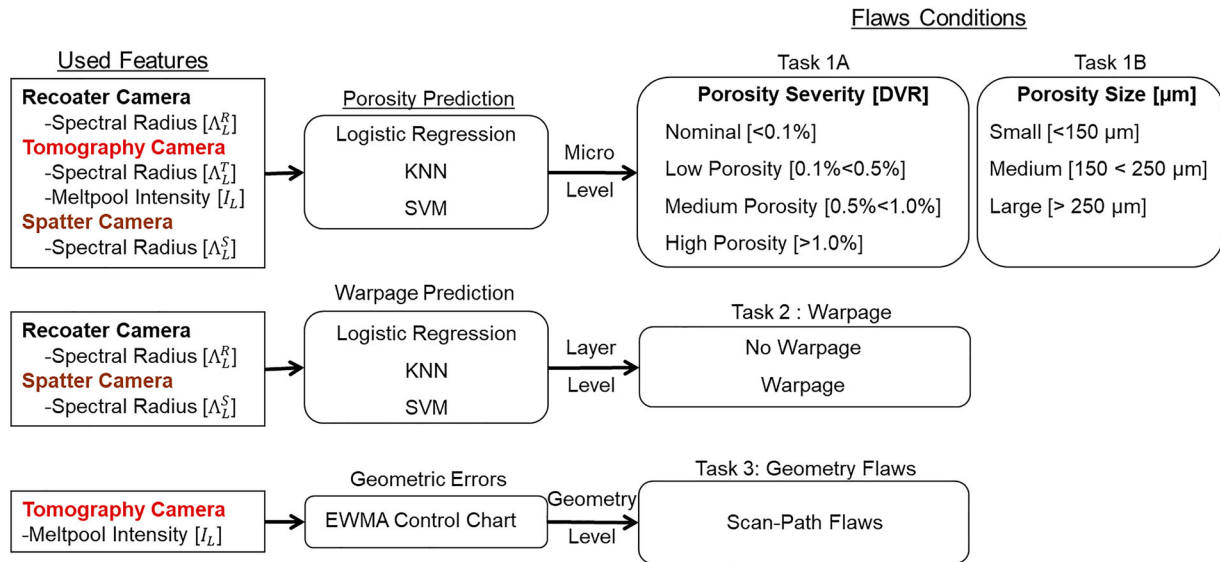


**Figure 11.** Schematic of the approach used in this work to detect micro-, layer- and geometry-level flaws. The three spectral radii ( $\Lambda_L^R$ ,  $\Lambda_L^T$ ,  $\Lambda_L^S$ ), along with the meltpool intensity ( $I_L$ ) are used as inputs to simple machine learning models to detect porosity, warpage and scan-path errors.

consequential in porosity detection in our prior works (Gaikwad et al. 2022).

The four features were used as inputs to simple machine learning models, such as K-nearest neighbours (KNN) and support vector machine (SVM) for detecting porosity severity, pore size and warpage. A statistical process control chart was used to detect the geometric level of flaws of incorrect scan paths.

The prediction fidelity for classifications level and type of porosity is quantified in terms of the F-score (Smoqi et al. 2022). The level of porosity is stratified into four levels, and the type of porosity is categorised into three levels.

Referring to Figure 11, data from all three sensors were used for detecting micro-scale porosity; data from only two sensors, recoater and spatter camera, were sufficient when detecting layer level warpage; and data from only the tomography sensor was needed for detecting geometric deviations. In this work, all flaw detection was performed on a layer-by-layer basis for each part. The specific X-Y region on a layer in which the flaw occurred was not detected, only that a specific layer on a part contains the detected flaw.

To attain prediction fidelity F-score  $> 90\%$ , porosity prediction required all four features; layer-level warpage flaw detection required two features (recoater  $\Lambda_L^R$  and spatter imaging  $\Lambda_L^S$ ); and geometry-level scanning errors required only one feature (NIR meltpool intensity,  $I_L$ ). In other words, the number and resolution of sensors required is inversely proportional to the scale of flaw formation to be detected.

### 3.5.2. Model training, testing and validation

After materials characterisation, an equal number of each of the three types of flaws (porosity, warpage and geometric) were selected for model training and testing to avoid bias due to an imbalanced data set. Machine learning models are trained to classify porosity into four levels based on X-ray CT defect volume ratio (DVR): nominal with  $<0.1\%$  DVR; low porosity with  $0.1\% < \text{DVR} < 0.5\%$ ; medium porosity with  $0.5\% < \text{DVR} < 1.0\%$ ; and high porosity with  $\text{DVR} > 1.0\%$ .

Likewise, pore size is classified into three levels based on pore diameter ( $d$ ):  $d < 150 \mu\text{m}$ ;  $150 \mu\text{m} < d < 250 \mu\text{m}$  and  $d > 250 \mu\text{m}$ . The smallest pore size of  $150 \mu\text{m}$  is in accordance with the resolution of the X-ray CT performed which had a voxel size of  $25 \mu\text{m}$ . Warpage and geometry-level flaws are both treated as a binary classification problem, i.e. warpage vs. no warpage.

In this work, 267 data points per pore severity level were randomly selected (1064 data points). Of these data sets, 80% of the data (213 data points per level) were used to train the machine learning models and the remaining 20% (54 data points per level) were used for testing. The results were subsequently validated with data obtained from a separate build plate (Figure 5 (b)) which had identical geometries and similar laser powers, but with part location rotated  $180^\circ$  to account for potential positional affects. Results from the porosity prediction model are described in Section 4.1.

Similarly, the warpage model was trained on the 500 layers (500 data points) of the cone geometry  $\theta = 35^\circ$ , as this was the geometry with the most observable warpage. The warpage model was then tested and



validated on all the cone, overhang and lattice structures from all three build plates. Finally, the scan path error EWMA control chart was designed on the nominal geometries with no errors and then tested on all other geometries. We note that only the lattice structure contained this scan path errors. Results from the warpage and scan path error models are described in detail in Sections 4.2 and 4.3 respectively.

## 4. Results

### 4.1. Porosity prediction

#### 4.1.1. Porosity measurements

##### (a) Cone

For cone-shaped parts processed under fixed conditions, i.e. with a nominal laser power  $P = 230$  W, the porosity was less than 0.01% (defect volume ratio, DVR). The porosity type and distribution observed using optical microscopy and X-ray CT for the dynamic-processed cone-shaped parts is shown in Figure 12. In contrast to the fixed processed cone, the dynamic-processed cone with a  $\theta = 35^\circ$  inclination angle has a DVR greater than 1.0%.

Porosity increases substantially when the laser power was reduced to  $P = 160$  W. For the dynamic-processed cone with a  $\theta = 40^\circ$  the DVR is  $\sim 0.6\%$ . Optical micrography reveals that porosity in the dynamic-processed cone is of the lack-of-fusion type (Snow, Nassar, and Reutzel 2020). Lack-of-fusion porosity results from insufficient consolidation of molten powder material owing to low energy input.

In this work, no keyhole porosity was observed with X-ray CT or optical microscopy in either the dynamic- or fixed-processed geometries. Indeed, the variation in pore diameter observed in this work is too large to be considered keyhole porosity. It is therefore reasonable to assume lack-of-fusion at low laser power, and spatter-induced porosity at high laser power (230 W).

Continuing with the analysis, the layer-by-layer mapping of porosity for the dynamic-processed cones is shown in Figure 13(a, b). The severity of porosity increases significantly in excess of 0.5% DVR when the power is reduced to 160 W, and is exacerbated when the power is further reduced to 120 W.

From this porosity data, we stratified the severity of porosity into four categories as follows, nominal porosity  $< 0.1\%$  DVR per layer; low porosity  $0.1\% - 0.5\%$  DVR per layer; medium porosity  $0.5\% - 1.0\%$  DVR per layer; and high porosity  $> 1.0\%$  DVR per layer. From Figure 13(a, b) we observe that the pore severity is a function of geometry as well as energy density. The cone with  $\theta = 35^\circ$  cone has significantly more porosity at  $P = 120$  W compared to the  $\theta = 40^\circ$  counterpart.

The pore size is mapped as a function of layer height for the dynamic cones in Figure 13(c, d) for  $\theta = 35^\circ$  and  $\theta = 40^\circ$ , respectively. The pore diameter increases in size when the power is decreased. This is because, as the laser power decreases, the overall energy density ( $E_v$ ) decreases as well. At low energy densities,  $E_v < 63 \text{ J}\cdot\text{mm}^{-3}$ , the powder particles are unable to fully fuse, forming the lack-of-fusion porosity observed in these samples (Snow, Nassar, and Reutzel 2020).

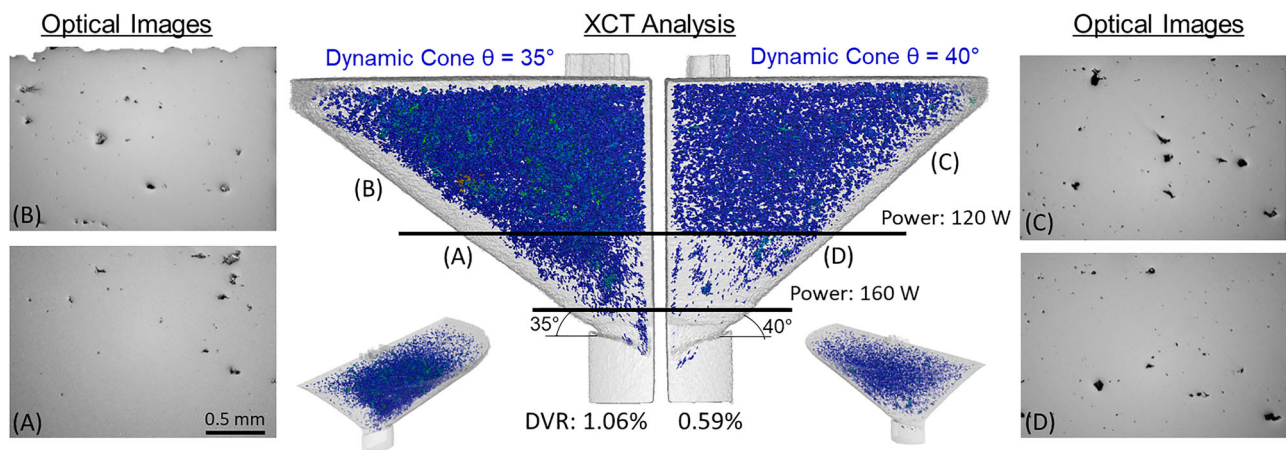


**Figure 12.** Porosity analysis for the dynamic-processed cone parts. (middle) X-ray CT shows that porosity increases significantly when the laser power is reduced to 160 and 130 W from the nominal 230 W. Further, optical micrographs reveal that the porosity is of the lack-of-fusion type.

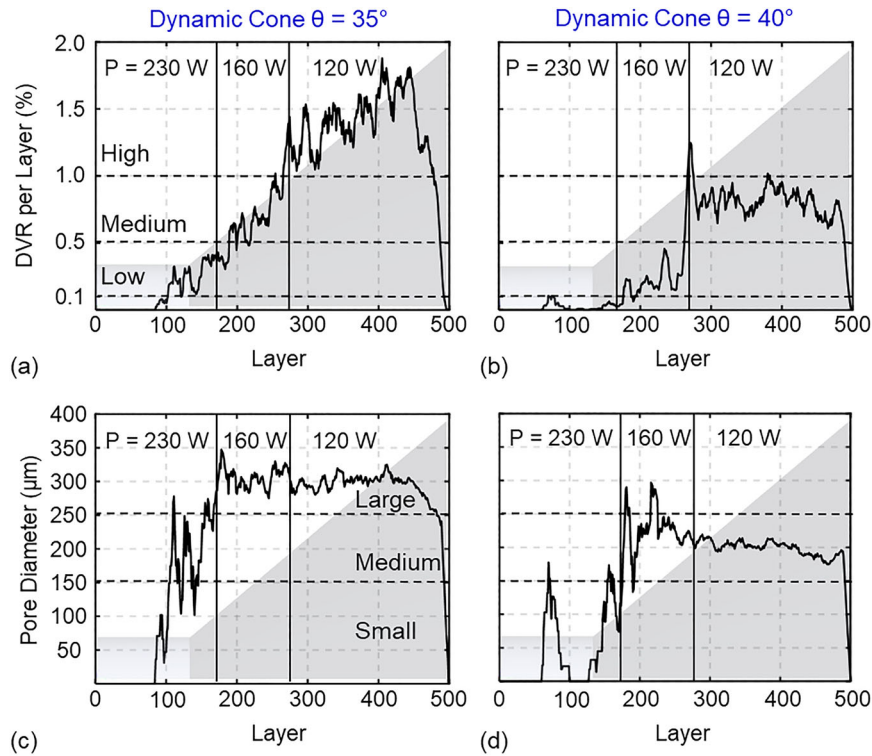


**Figure 13.** (a) and (b) Percent porosity (DVR) per layer observed for the two dynamic cone parts,  $\theta = 35^\circ$  and  $\theta = 40^\circ$  respectively. The corresponding levels of classification are annotated. Note the significant increase in percent porosity (DVR) when the laser power is reduced to  $P = 160$  W and further to  $P = 120$  W. Further the cone with  $\theta = 35^\circ$  has significantly more porosity at  $P = 120$  W compared to  $\theta = 40^\circ$ . (c) and (d) Pore diameter as a function of layer number. Porosity of the lack-of fusion type with diameter ranging from  $d < 100 \mu\text{m}$  to  $d > 300 \mu\text{m}$  are observed.

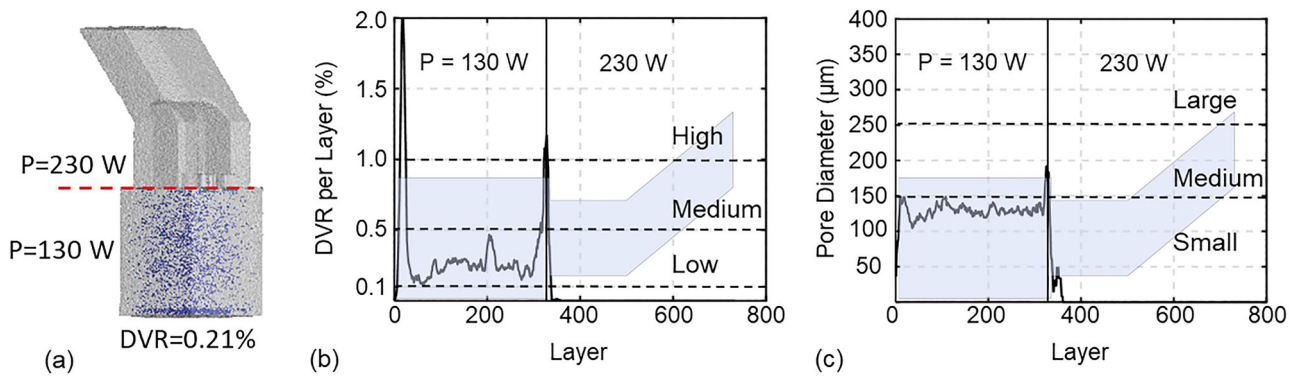


**Figure 14.** (a) Visual of the X-ray CT results done in this work for this overhang part. (b) Percent porosity per layer observed for the fixed overhang geometry. The corresponding levels of classification are annotated. Note the significant increase in percent porosity in the lower cuboid section where the laser power was set to 130 W. (c) Pore diameter as a function of layer number. Porosity of the lack-of fusion type with diameter less than  $150 \mu\text{m}$  is observed.

#### (b) Overhang

Consistent with the observation for the cone-shaped parts, lack-of-fusion porosity was also observed in the overhang parts when the laser power was reduced below  $P = 230$  W to  $P = 130$  W. Shown in Figure 14(a) are the X-ray CT results for the only overhang part

with detectable levels of porosity. The porosity in this sample occurs in the first 10 mm when  $P = 130$  W.

The layer-by-layer analysis of the porosity is shown in Figure 14(b) in terms of DVR. Note that relative to the cone, low levels of porosity (DVR  $< 1\%$ ) were observed in the overhang sample. Shown in Figure 14(c) is the visualisation of pore diameter observed in the overhang

sample. All pores observed were lack-of-fusion pores with  $d < 150 \mu\text{m}$ .

#### 4.1.2. Correlation of sensor signatures to porosity severity and pore size

Next, in Figure 15, we correlated the four sensor signatures to the level of porosity severity and size. The four features are: spectral radius of the spatter camera images ( $\Lambda_L^S$ ); spectral radius from the recoater camera images ( $\Lambda_L^R$ ); spectral radius from the tomography camera images ( $\Lambda_L^T$ ); and relative meltpool intensity from the tomography camera ( $I_L$ ).

From Figure 15, it is observed that the spectral radius for the spatter ( $\Lambda_L^S$ ) and tomography ( $\Lambda_L^T$ ) camera image decreases as the porosity level increases. This is because as lack-of-fusion porosity forms, the image data becomes less homogenous, which causes the spectral radius number to decrease. Likewise, the normalised meltpool intensity ( $I_L$ ) decreases with increase in porosity level (severity) as the incident energy density decreases due to the reduction in laser power.

The interaction amongst sensor signatures for the four levels of porosity is visualised in the form of a

scatter plot shown in Figure 16. In all plots, there is a clear correlation between lower spectral radii and higher levels of porosity severity. However, there is significant overlap in the data, thus necessitating the use of machine learning to predict the porosity severity.

The interaction amongst sensor signatures to pore size is visualised in the form of four scatter plots shown in Figure 17. In all scatter plots in Figure 17, prominent clustering of features relative to the pore diameter is evident, and the overlap is not as considerable as that observed in the context of porosity severity (Figure 16). Accordingly, simple logistic regression would perform at par with machine learning for classifying pore size.

#### 4.1.3. Machine learning

Next, the four features:  $\Lambda_L^T$ ,  $\Lambda_L^S$ ,  $\Lambda_L^R$  and  $I_L$  were used as inputs to a logistical regression model, and three simple machine learning models – k-nearest neighbours (KNN), support vector machine (SVM) and shallow artificial neural networks (ANN). The statistical regression model is used as a baseline as it does not involve an active learning step (Dreiseitl and Ohno-Machado 2002).

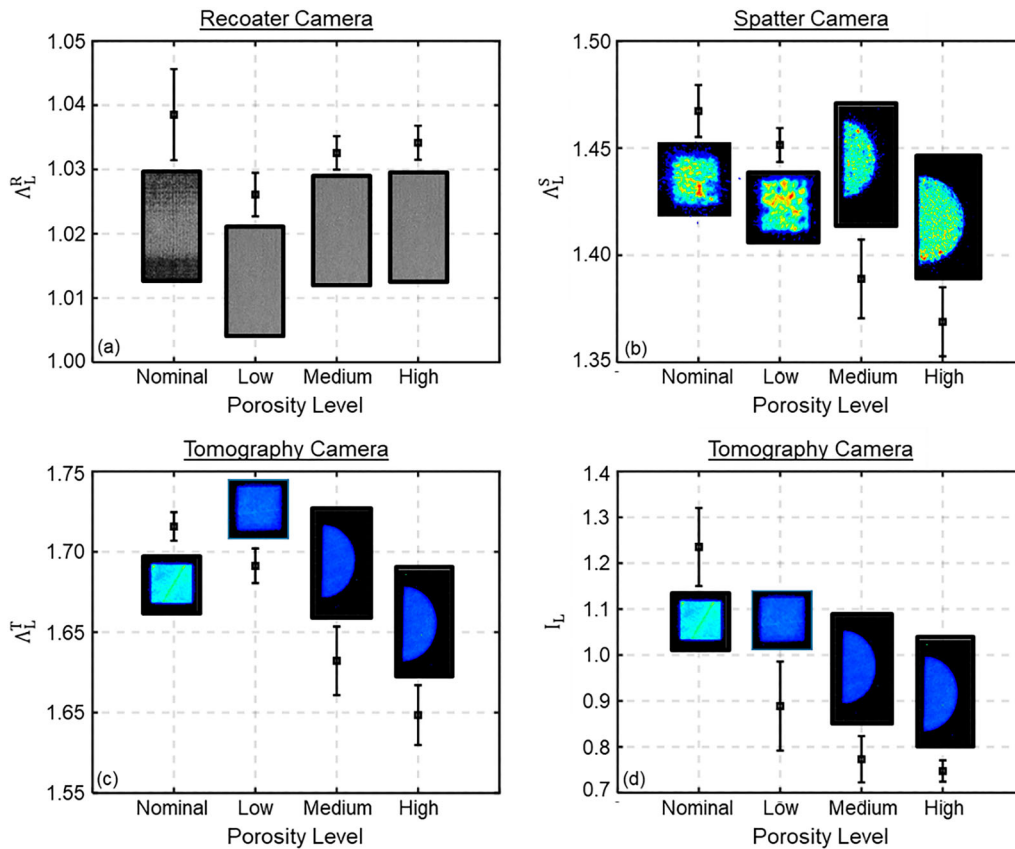


**Figure 15.** The behaviour of the four process signatures as a function of porosity level. (a-c): The recoater spectral radius ( $\Lambda_L^R$ ) does not change significantly with pore level, however, the spectral radii for both the spatter camera ( $\Lambda_L^S$ ) and tomography camera ( $\Lambda_L^T$ ) decreases significantly as the level of porosity increases. (d) Meltpool intensity ( $I_L$ ) decreases with increasing porosity severity.

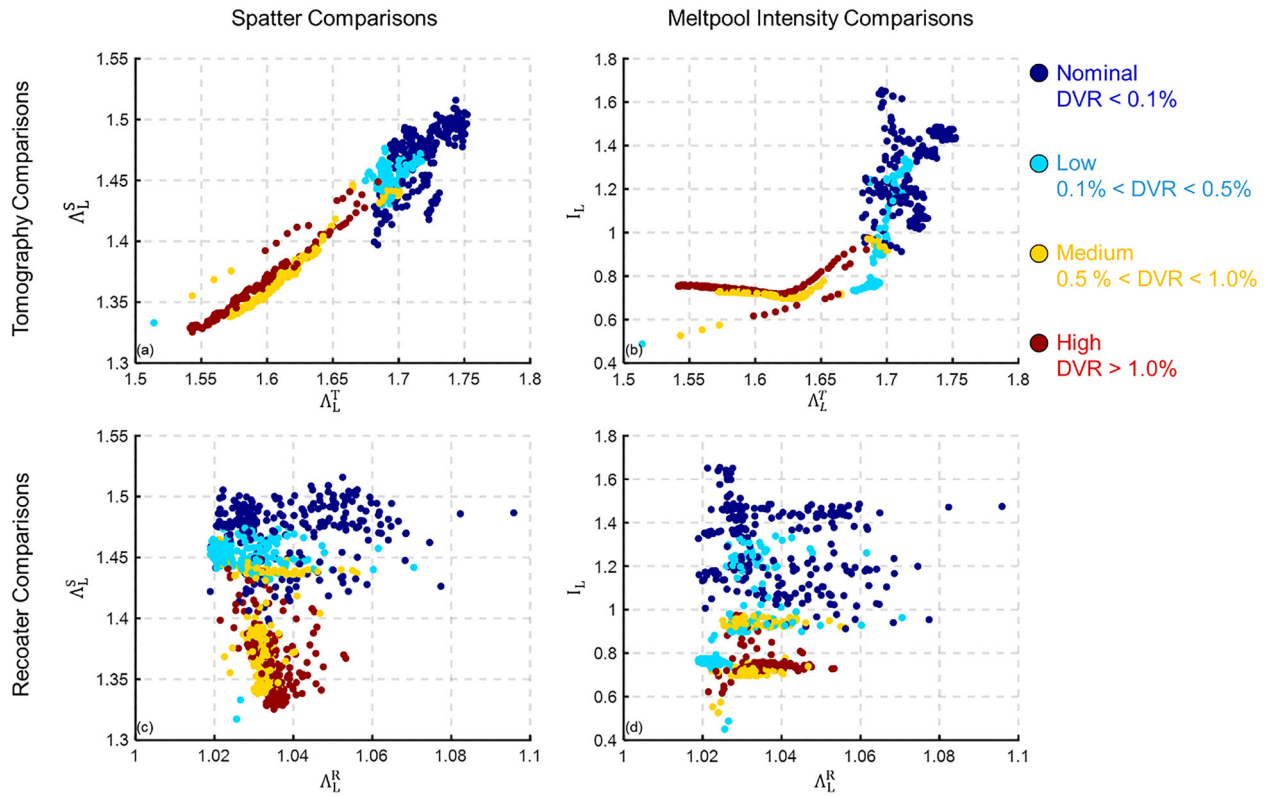


**Figure 16.** Visualisation of interaction between sensor signatures for various levels of porosity severity. In the visualisation there is a large overlap in the high and medium levels of porosity sensor signatures.

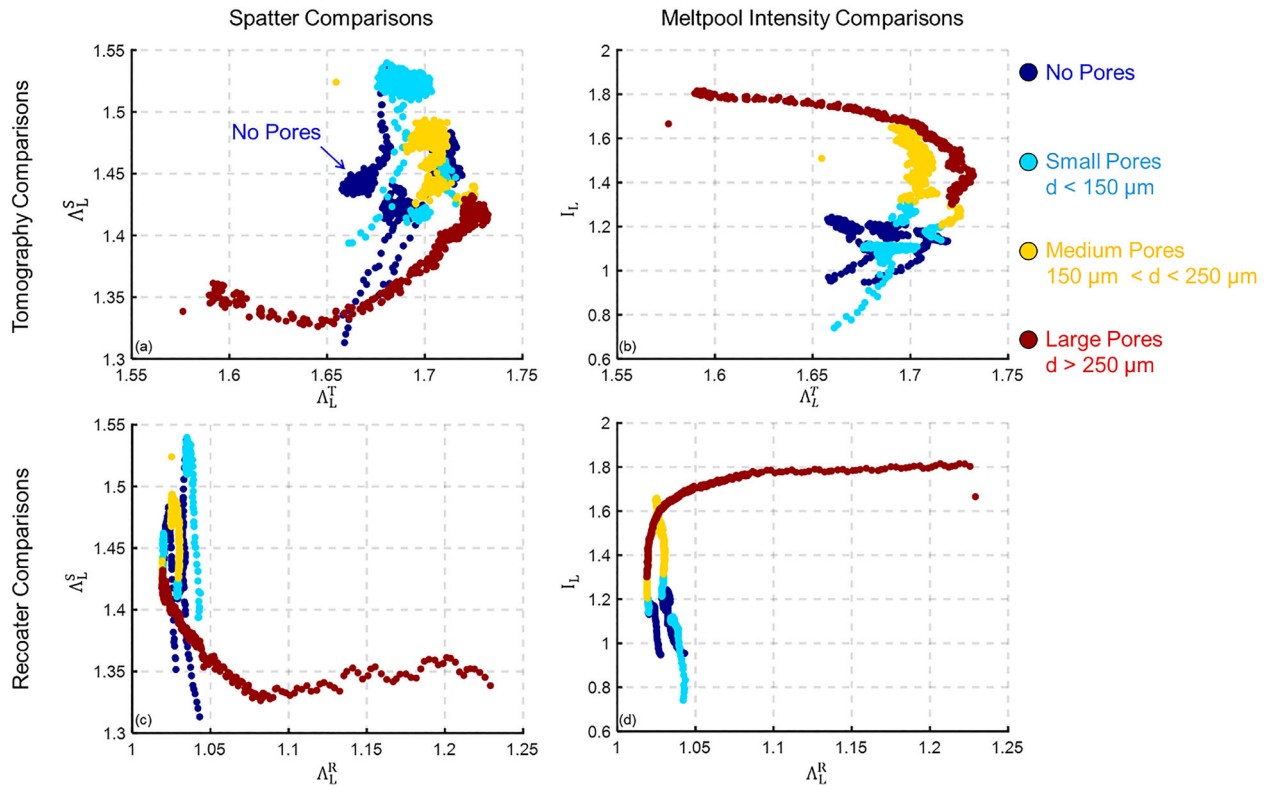


**Figure 17.** Visualisation of interaction between sensor signatures for various levels of pore diameter. In the visualisation, no singular 2D scatter plot has a perfect separation of the data.

**Table 4.** The performance of the four models used in the work for prediction of porosity level and size, along with the false positive and false negative rates. A total of 1068 data points were used for training and 234 data points were used for testing. The number in the parenthesis is the standard deviation (STD) over 10 train/test iterations.

Model		Logistic Regression	KNN	SVM	ANN
F-Score (STD)	Pore Severity	77.3% (2.48%)	92.3% (1.75%)	93.5% (1.68%)	91.4% (2.44%)
	Pore Size	92.6% (1.70%)	98.8% (0.60%)	98.6% (0.46%)	99.6% (0.3%)
False Positive Rate	Pore Severity	7.8%	2.6%	1.6%	2.8%
	Pore Size	2.4%	0.3%	0.6%	0.3%
False Negative Rate	Pore Severity	22.7%	7.8%	4.8%	8.5%
	Pore Size	7.8%	0.9%	1.7%	0.9%

**Table 5.** The confusion matrix for pore severity classification from the SVM model resulting in F-score > 93%. Out of 234 data points there were only 13 misclassifications.

Actual Severity Values	Predicted Porosity Severity Values			
	Nominal Porosity (DVR < 0.1%)	Low Porosity (0.1 < DVR < 0.5%)	Medium Porosity (0.5 < DVR < 1%)	High Porosity (DVR > 1%)
Nominal Porosity (DVR < 0.1%)	<b>61</b>	2	1	0
Low Porosity (0.1 < DVR < 0.5%)	1	<b>58</b>	3	0
Medium Porosity (0.5 < DVR < 1%)	0	2	<b>51</b>	0
High Porosity (DVR > 1%)	0	2	2	<b>51</b>

**Table 6.** The confusion matrix for pore diameter classification from the SVM model resulting in F-score > 98%. Out of the 240 data points there was only 1 misclassification.

Actual Severity Values	Predicted Porosity Severity Values			
	No Pores	Small Pores ( $d < 150 \mu\text{m}$ )	Medium Pores ( $150 < d < 250 \mu\text{m}$ )	Large Pores ( $d > 250 \mu\text{m}$ )
No Pores	<b>60</b>	1	0	0
Small Pores ( $d < 150 \mu\text{m}$ )	0	<b>66</b>	0	0
Medium Pores (150 < $d < 250 \mu\text{m}$ )	0	0	<b>53</b>	0
Large Pores ( $d > 250 \mu\text{m}$ )	0	0	0	<b>60</b>

The ANN used in this work was a shallow multi-layer perceptron (MLP) with only two hidden layers, each layer containing 15 neurons using the tangent sigmoid activation function. We acknowledge that performance of the ANN could be enhanced by adding more hidden layers, at the risk of losing model interpretability and potential overfitting. All models were trained and tested using the 80–20 schema described previously in Section 3.5 with 10-fold cross validation and Bayesian hyperparameter tuning.

The model results are reported in terms of the F-score, false positive rates and false negative rates (Table 4). The number in the parenthesis in Table 4 is the standard deviation over the ten trials. The SVM model predicts the level of porosity with ~93% fidelity (F-score) with false positive and false negative rates of 1.6% and 4.8% respectively using a radial basis kernel function. In comparison the statistical logistic regression model could only classify the level of porosity at 77.4% fidelity, justifying the need for machine learning. A representative confusion matrix from the SVM model is shown in Table 5. We

note that from the total of 234 data points used for testing there were only 13 misclassifications.

A visualisation of SVM model performance in the context of level of porosity severity is presented in Figure 18(a) and (b) for the overhang geometry and cone geometry with  $\theta = 35^\circ$ . For the two different geometry types, the SVM model successfully predicts the change in level of porosity due to change in laser power.

In addition to the prediction of the level of porosity (porosity severity), the size of pore, in terms of pore diameter, for these samples was also performed. The size of pore was classified between 3 different sizes, in layers that contained porosity: small diameter ( $d < 150 \mu\text{m}$ ), medium diameter ( $150 < d < 250 \mu\text{m}$ ) and large diameter ( $d > 250 \mu\text{m}$ ). The results are summarised in Table 4 and Table 6.

The prediction of pore diameter was performed using the previously described 80–20 train-test strategy. The SVM model predicted the pore size with an F-score of 98.64% (0.46%). We also note that statistical logistic regression has an appreciable score of 92.65% (1.70%)

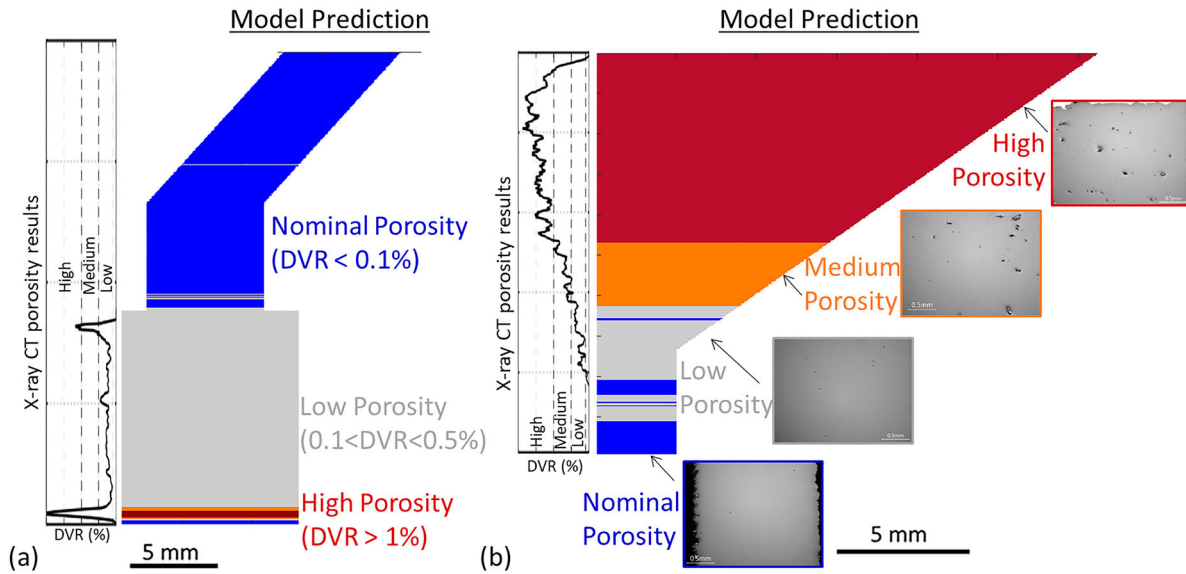


**Figure 18.** Visualisation of the SVM model's porosity severity prediction for the overhang (a) and cone geometry  $\theta = 35^\circ$  (b). The model successfully predicts the porosity in both of these samples.

for predicting pore size, which implies that the classification of pore size is a simpler problem, when using the proposed feature set, compared to level of porosity (pore severity). As noted in the context of Figure 17, the four features cluster in a prominent matter contingent on the size of pore.

Thus, simple machine learning models are capable of linking the extracted sensor signatures, discussed in Figures 16 and 17, to both pore size and severity. In

other words, pragmatic, physically intuitive process signatures, when coupled with simple machine learning models are capable of detecting flaw formation with high levels of statistical fidelity (F-score > 93%).

#### 4.2. Warpage prediction

As observed in Figure 19(a, b), respectively, both the cone with angle of inclination  $\theta = 35^\circ$  and the

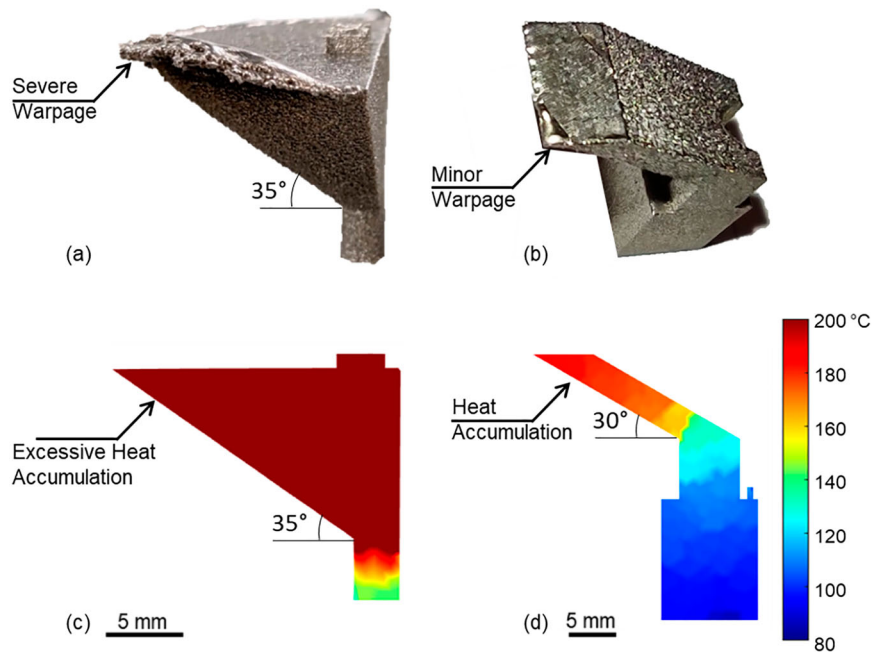


**Figure 19.** Both an inverted cone (a) and an overhang geometry (b) had produced under constant power P-230 W depicted significant warpage. Thermal simulation of the cone geometry at an inclination of  $35^\circ$  (c) and the overhang geometry at  $30^\circ$  (d) show heat accumulation at the top of the part that could lead to thermal distortion.

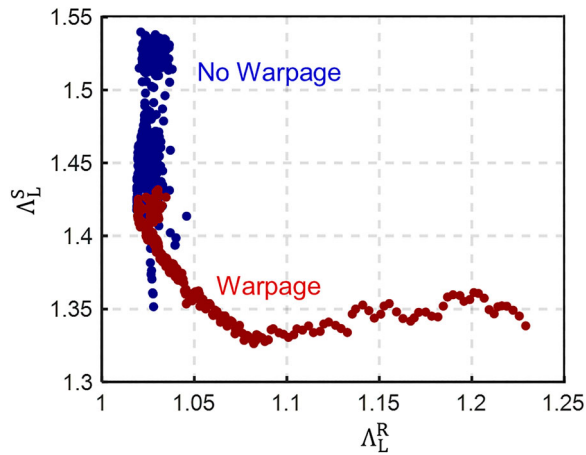


**Figure 20.** Visualisation of the warpage and non-warpage states are interpreted by the high-speed and recoater sensor. Both sensors are needed to see separation in the data.

overhang ( $\theta = 30^\circ$ ) processed under fixed laser power of 230 W, were afflicted with significant warpage. We note that the dynamic-processed cones did not warp. This warpage is on account of excessive heat accumulation leading to the thermal distortion of the parts built under fixed processing parameters. Indeed, a thermal simulation using our previously published thermal models shown in Figure 19(c, d) predicted heat build-up (accumulation) in these parts (Yavari et al. 2021b).

Another SVM model using the radial basis kernel function, similar to the one used to for the prediction of porosity in Section 4.1, was deployed for prediction of warpage. Noting that this is a two-fold classification problem – warpage vs. no warpage. During analysis it was observed that only two spectral radii,  $\Lambda_L^S$  and  $\Lambda_L^R$

from the spatter and recoater cameras respectively, were sufficient to detect warpage. Since warpage is a considerably larger scale phenomena than porosity formation, a few process signatures are sufficient. These process signatures ( $\Lambda_L^S$  and  $\Lambda_L^R$ ) are correlated with warpage shown in Figure 20; we note that the data encompasses both overhang and cone geometries. From Figure 20, for parts with significant warpage, the  $\Lambda_L^S$  is generally below 1.45 and the  $\Lambda_L^R$  is generally greater than 1.03. However, there is considerable overlap between the two monitoring features that require simple machine learning models to precisely ascertain the regions of warpage.

Further to test model transferability, only data from the cone was leveraged for training the SVM model and subsequently used as-is for predicting warpage in the more complex overhang part, Figure 21. The SVM model successfully captured the relatively subtle warpage at the top few layers of the overhang part. We note that sporadic appearance of warpage at the top layers is due to the self-healing nature of the LPBF process (Ulbricht et al. 2021). Further, the apparent false detection in the first few layers is associated with poor recoating. The recoater blade is not level with the build plate for the first 5–10 layers – a common problem in LPBF.

Continuing with the analysis, the warpage detection model was extended beyond the cone and overhang geometries to the complex lattice structure, shown in Figure 22. The lattice structure had multiple instances of warpage wherein warpage exceeded the layer height ( $T = 30 \mu\text{m}$ ) and the part surface was raised above the freshly raked powder (super elevation).

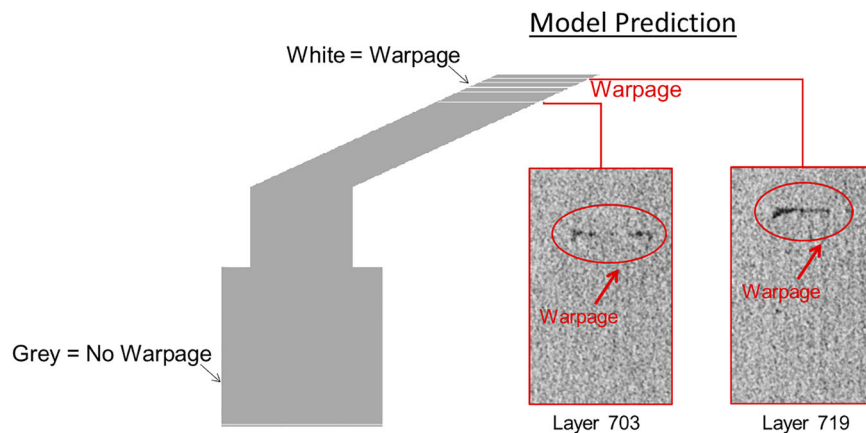


**Figure 21.** In the overhang part, white regions demarcate layers of predicted warpage. The warpage detection model trained on the cone geometry was successfully as-is to the overhang geometry. The spectral radius signatures from the recoater ( $\Lambda_L^R$ ) and spatter ( $\Lambda_L^S$ ) imaging sensors were sufficient for detection of warpage.

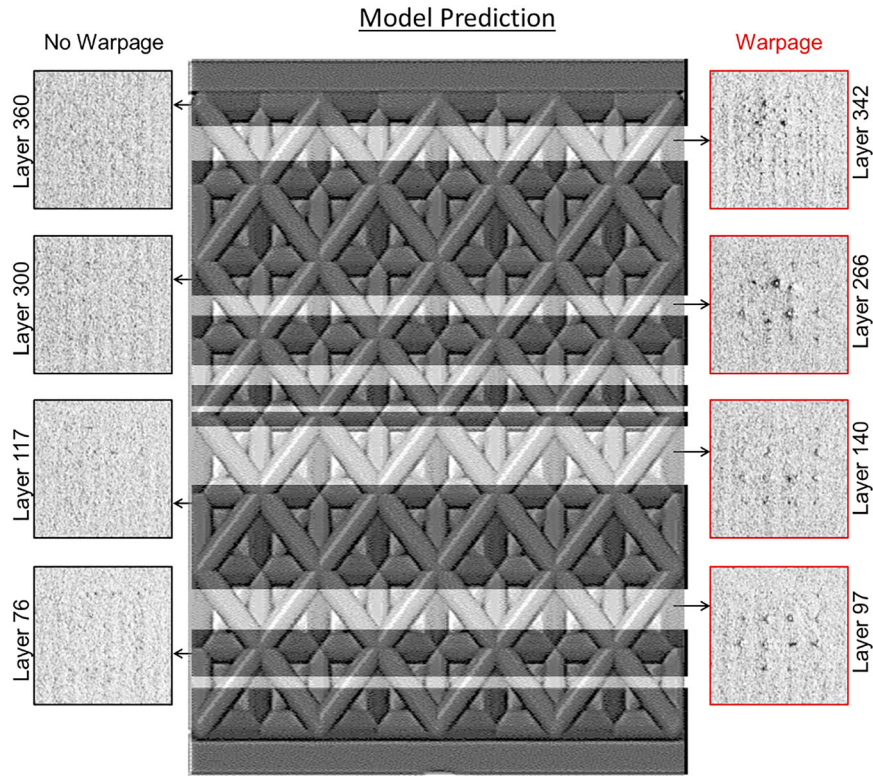


**Figure 22.** The SVM model when transferred successfully detects warpage in the complex lattice structure at layers demarcated by the white stripes.

### 4.3. Geometry error detection

X-ray CT analysis showed that the lattice structure contained flaws due to scanning errors. As depicted in Figure 23, these scanning errors cause significant deviation in the part geometry from the CAD design. Incorrect scanning was observed in the lattice structure when the body-centered lattice structure was repeated in the build direction. In practice, laser scanning errors may occur for a variety of reasons, including improper slicing of the CAD model resulting in poor resolution, errors in the scan path generation software, and lens aberrations (Gaikwad et al. 2022; Yavari et al. 2021a).

In this work, regions of improper scanning resulted in excess melting of material that covered the gaps between the lattice edges. These regions of scanning errors were correlated with prominent variation in the meltpool intensity ( $I_L$ ). Shown in Figure 23 is the layer-by-layer gradient ( $\frac{d}{dt} I_L$ ) compared to the layers in which improper scanning occurred.

The gradient of the mean meltpool intensity ( $\frac{d}{dt} I_L$ ) was monitored in an exponentially weighted moving

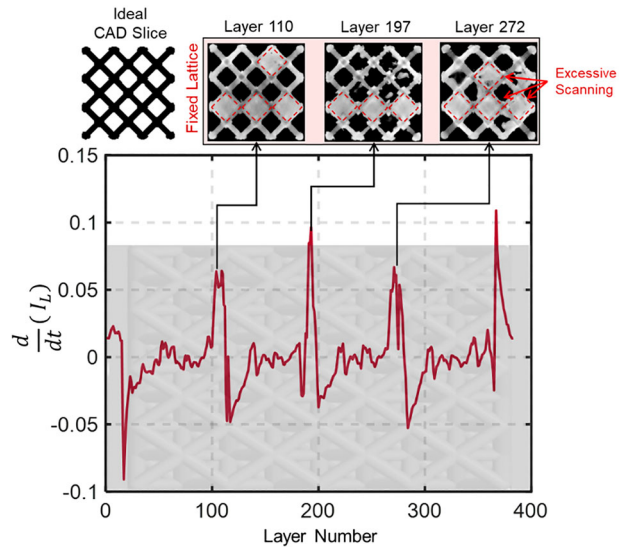


**Figure 23.** Both lattice structures depicted scan path-related errors that causes additional material to be melted that covers the gaps in the lattice structure (overmelting). These scan path-related errors are correlated to spikes in the gradient of the meltpool intensity ( $\frac{d}{dt} I_L$ ) obtained from the tomography sensor.



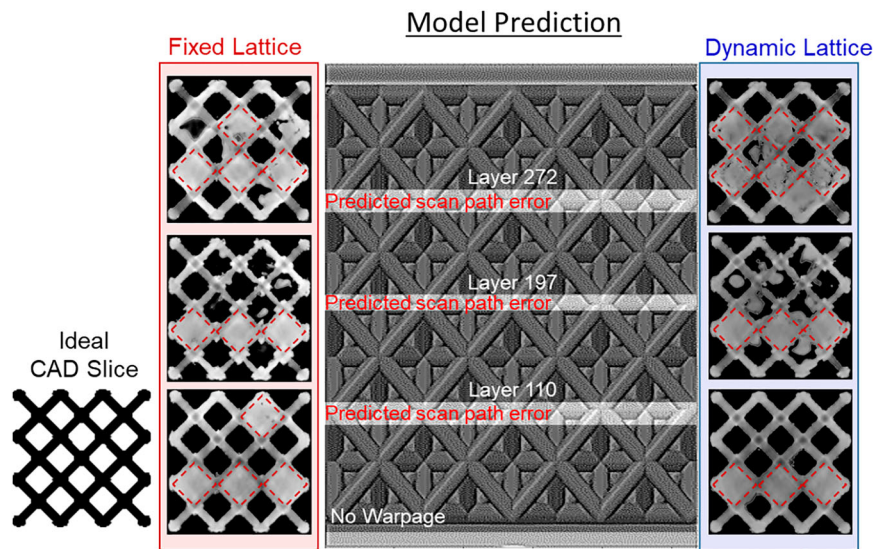


**Figure 24.** Detection of geometry errors due to scan path errors using the EWMA control chart. The white shaded layers indicate points at which the sensor signatures cross the control limits due to inaccurate scan paths.

average (EWMA) statistical control chart, described in Section 3.4 Equation (5) (Ramirez and Ramírez 2018). The control limits were set to  $\pm 3$  deviations obtained from the flaw-free overhang parts.

As observed in Figure 24, when there is a geometric related error the gradient of the mean meltpool intensity ( $\frac{d}{dt} I_L$ ) exceeds the upper control limit of the EWMA control chart. This is affirmed in the case of both the fixed and dynamic-processed lattice structures. Incidentally, both type of lattice processing resulted in flaws on the same layers, layer 110, 197 and 272.

This scanning error was traced to an inherent deficiency in the slicing software, which could not accommodate the computational complexity associated with a lattice structure. The slicing error further created scan path inconsistencies that caused the laser to melt the powder in the

gaps in the lattice structure. The scan path errors are observed on the layers where the base lattice structure repeated. There are four replications of the base lattice structure, hence there are three layers where scan path errors were observed in the X-ray CT data.

#### 4.4. Model transferability

A third build plate (Figure 5(b), Section 2.2) was manufactured to ascertain the transferability of the proposed approach to a different build plate with varying part locations, and further quantify the Type I (false positive rate) error.

To test the robustness of the approach to changes in process conditions, the dynamic-processed cone was reduced to 160 W at 8 mm build height, instead of at

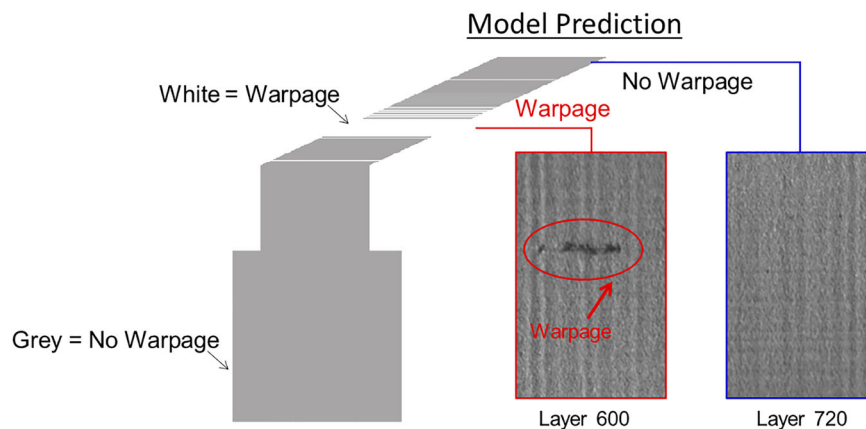


**Figure 25.** Model performance for the validation build. White demarcates layers of warpage found on this overhang part. The steepest overhang sample warps for about 50 layers near the top of the part and then self-heals in the last few layers.

5 mm in the first build plate design (Figure 6). In addition, to affirm the robustness of the approach to variation in part location, the part locations on the build plate were rotated by 180°, as shown and discussed in Figure 5(b).

No perceivable flaw formation was observed in the build plate in terms of porosity and warpage errors discovered in the first two build plates. This is because the change in the direction of the gas flow relative to the parts significantly influenced their cooling behaviour (Wirth et al. 2021). In other words, even a slight change in processing conditions may significantly affect part quality, thus affirming the need for continuous in-process monitoring.

We noted minor warpage in only one overhang shape. The layer-level warpage model created for the first build plate was deployed on this overhang sample. The model successfully detected the layers at which incipient warpage occurs in the overhang part at layer 600. Figure 25 shows the resultant warpage prediction for the overhang sample from the SVM model. The noticeable amount of warpage in the vicinity of layer 600 was successfully detected.

Additionally, the SVM-based porosity prediction model (Section 4.1) was implemented on the overhang and cone geometries on the validation build plate to measure the Type I (false positive rate) of the trained models. The false positive rate for the porosity prediction model was less than 1.5% when the prior SVM model was implemented on the validation build plate. This false alarm rate, which is similar to the false alarm rate found during training and testing on the first build plate (1.6%), indicates that the model can be successfully transferred to a different build plate under different processing conditions without loss of model fidelity. We acknowledge that the model would need further testing under build conditions resulting in excessive porosity to measure the false negative rate and F-score.

## 5. Conclusions

Process monitoring in laser powder bed fusion (LPBF) is currently limited to the detection and identification of one type of flaw with data acquired from only one type of sensor. For practical viability, a monitoring solution must be capable of detecting multi-level flaws transcending micro-scale, meso-scale and macro-scale. Furthermore, the monitoring performance of the approach should not degrade when transferred across builds, part shapes, orientations and locations.

Accordingly, this work extends the status quo of process monitoring and flaw detection in LPBF to a

more practical level with an approach that can combine (fuse) data from multiple, heterogeneous sensing modalities to detect multiscale flaw formation. Based on data from three builds consisting of 66 total parts (Nickel Alloy 718) we demonstrate that the proposed approach is capable of detecting multiscale flaws ranging from porosity at the micro-scale, warpage at the meso-scale, and geometry-related errors at the macro-scale. Further, the approach is agnostic to different part shapes, locations and orientations (build layout).

Specific conclusions are as follows:

- (1) Data from three types of thermo-optical imaging sensors, a spatter imaging camera, near infrared tomographic camera, and a recoater camera were acquired during the LPBF of three build plates consisting of 22 parts each (Nickel Alloy 718), encompassing four different types of geometries.
- (2) A spectral graph signal analysis approach was developed and applied to extract signatures from the three imaging sensors. The approach reduces the high dimensional data from the imaging sensors into a single scalar number called the Laplacian graph spectral radius. As few as four process signatures resulting from the signal analysis approach were used as inputs to simple machine learning algorithms, such as k-nearest neighbours, support vector machine, and (shallow) artificial neural networks.
- (3) The proposed approach successfully detected flaws across three scales – porosity, warpage and part geometry in different part shapes and build layouts. For example, the statistical fidelity of porosity detection exceeded 93% (F-score); the false positive rate was less than 1.6% and the false negative rate was less than 4.8%.
- (4) The number of features required for effective process monitoring depends on the scale of flaws. Detection of micro-scale porosity required all four features, whereas, detection of mesoscale warpage and geometry-related error was accomplished with two features and one feature, respectively. In other words, the resolution and type of sensor data is matched to the scale of flaw formation.

This work thus takes the first step towards shape agnostic detection of multiscale flaws in LPBF using heterogeneous sensor data. Our future works will explore not only detection but also closed-loop correction of flaws in LPBF.

## Acknowledgments

The characterisation work performed at the Nebraska Nanoscale Facility: National Nanotechnology Coordinated Infrastructure under award no. ECCS: 2025298, and with support from the Nebraska Research Initiative through the Nebraska Center for Materials and Nanoscience and the Nanoengineering Research Core Facility at the University of Nebraska-Lincoln.

## Disclosure statement

No potential conflict of interest was reported by the author(s).

## Funding

Pralhada Rao acknowledges funding from the Department of Energy (DOE), Office of Science, under Grant number DE-SC0021136, and the National Science Foundation (NSF) [Grant numbers CMMI 1752069/CMMI 2309483, CMMI-1719388, CMMI-1920245, CMMI-1739696, PFI-TT 2044710, ECCS 2020246] for funding his research programme. H. Scot Halliday acknowledges funding from the NSF for Award #1840138 funding the NTU Center for Advanced Manufacturing.

## References

- Blakey-Milner, B., P. Gradl, G. Snedden, M. Brooks, J. Pitot, E. Lopez, M. Leary, F. Berto, and A. du Plessis. 2021. "Metal Additive Manufacturing in Aerospace: A Review." *Materials & Design* 209: 110008. doi:10.1016/j.matdes.2021.110008.
- Chen, H., S. Patel, M. Vlasea, and Y. Zou. 2022. "Enhanced Tensile Ductility of an Additively Manufactured AlSi10Mg Alloy by Reducing the Density of Melt Pool Boundaries." *Scripta Materialia* 221: 114954. doi:10.1016/j.scriptamat.2022.114954.
- Chung, F. R. 1997. *Spectral Graph Theory*. Fresno California: American Mathematical Society.
- DebRoy, T., H. L. Wei, J. S. Zuback, T. Mukherjee, J. W. Elmer, J. O. Milewski, A. M. Beese, A. Wilson-Heid, A. De, and W. Zhang. 2018. "Additive Manufacturing of Metallic Components – Process, Structure and Properties." *Progress in Materials Science* 92: 112–224. doi:10.1016/j.pmatsci.2017.10.001.
- Diegel, O., A. Nordin, and D. Motte. 2019. *Design for Metal AM, A Practical Guide to Design for Additive Manufacturing*, 121–155. Gateway East, Springer.
- Dreiseitl, S., and L. Ohno-Machado. 2002. "Logistic Regression and Artificial Neural Network Classification Models: A Methodology Review." *Journal of Biomedical Informatics* 35 (5): 352–359. doi:10.1016/S1532-0464(03)00034-0.
- Du Plessis, A., S. G. le Roux, J. Waller, P. Sperling, N. Achilles, A. Beerlink, J.-F. Métayer, M. Sinico, G. Probst, and W. Dewulf. 2019. "Laboratory X-ray Tomography for Metal Additive Manufacturing: Round Robin Test." *Additive Manufacturing* 30: 100837. doi:10.1016/j.addma.2019.100837.
- Everton, S. K., M. Hirsch, P. Stravroulakis, R. K. Leach, and A. T. Clare. 2016. "Review of in-Situ Process Monitoring and in-Situ Metrology for Metal Additive Manufacturing." *Materials & Design* 95: 431–445. doi:10.1016/j.matdes.2016.01.099.
- Gaikwad, A., B. Giera, G. M. Guss, J.-B. Forien, M. J. Matthews, and P. Rao. 2020a. "Heterogeneous Sensing and Scientific Machine Learning for Quality Assurance in Laser Powder bed Fusion – A Single-Track Study." *Additive Manufacturing* 36: 101659. doi:10.1016/j.addma.2020.101659.
- Gaikwad, A., F. Imani, H. Yang, E. Reutzel, and P. Rao. 2019. "In Situ Monitoring of Thin-Wall Build Quality in Laser Powder bed Fusion Using Deep Learning." *Smart and Sustainable Manufacturing Systems* 3 (1). doi:10.1520/SSMS20190027
- Gaikwad, A., R. J. Williams, H. de Winton, B. D. Bevans, Z. Smoqi, P. Rao, and P. A. Hooper. 2022. "Multi Phenomena Melt Pool Sensor Data Fusion for Enhanced Process Monitoring of Laser Powder bed Fusion Additive Manufacturing." *Materials & Design* 221: 110919. doi:10.1016/j.matdes.2022.110919.
- Gaikwad, A., R. Yavari, M. Montazeri, K. Cole, L. Bian, and P. Rao. 2020b. "Toward the Digital Twin of Additive Manufacturing: Integrating Thermal Simulations, Sensing, and Analytics to Detect Process Faults." *IJSE Transactions* 52 (11): 1204–1217. doi:10.1080/24725854.2019.1701753.
- Gordon, J. V., S. P. Narra, R. W. Cunningham, H. Liu, H. Chen, R. M. Suter, J. L. Beuth, and A. D. Rollett. 2020. "Defect Structure Process Maps for Laser Powder Bed Fusion Additive Manufacturing." *Additive Manufacturing* 36: 101552. doi:10.1016/j.addma.2020.101552.
- Gradl, P. R., D. C. Tinker, J. Ivester, S. W. Skinner, T. Teasley, and J. L. Bili. 2021. "Geometric Feature Reproducibility for Laser Powder Bed Fusion (L-PBF) Additive Manufacturing with Inconel 718." *Additive Manufacturing* 47: 102305. doi:10.1016/j.addma.2021.102305.
- Grasso, M., and B. M. Colosimo. 2017. "Process Defects and in Situ Monitoring Methods in Metal Powder bed Fusion: A Review." *Measurement Science and Technology* 28 (4): 044005. doi:10.1088/1361-6501/aa5c4f.
- Grasso, M., A. Remani, A. Dickins, B. M. Colosimo, and R. K. Leach. 2021. "In-situ Measurement and Monitoring Methods for Metal Powder Bed Fusion: An Updated Review." *Measurement Science and Technology* 32 (11): 112001. doi:10.1088/1361-6501/ac0b6b.
- Huang, D. J., and H. Li. 2021. "A Machine Learning Guided Investigation of Quality Repeatability in Metal Laser Powder bed Fusion Additive Manufacturing." *Materials & Design* 203: 109606. doi:10.1016/j.matdes.2021.109606.
- Ibrahim, Y., C. M. Davies, C. Maharaj, Z. Li, J. P. Dear, and P. A. Hooper. 2020. "Post-yield Performance of Additive Manufactured Cellular Lattice Structures." *Progress in Additive Manufacturing* 5 (2): 211–220. doi:10.1007/s40964-020-00128-4.
- Imani, F., A. Gaikwad, M. Montazeri, P. Rao, H. Yang, and E. Reutzel. 2018. "Process Mapping and In-Process Monitoring of Porosity in Laser Powder Bed Fusion Using Layerwise Optical Imaging." *Journal of Manufacturing Science and Engineering* 140 (10): 101009. doi:10.1115/1.4040615.
- Jin, Z., Z. Zhang, K. Demir, and G. X. Gu. 2020. "Machine Learning for Advanced Additive Manufacturing." *Matter* 3 (5): 1541–1556. doi:10.1016/j.matt.2020.08.023.
- Khairallah, S. A., A. T. Anderson, A. Rubenchik, and W. E. King. 2016. "Laser Powder-bed Fusion Additive Manufacturing:

- Physics of Complex Melt Flow and Formation Mechanisms of Pores, Spatter, and Denudation Zones." *Acta Materialia* 108: 36–45. doi:10.1016/j.actamat.2016.02.014.
- Kobir, M. H., R. Yavari, A. R. Riensche, B. D. Bevans, L. Castro, K. D. Cole, and P. Rao. 2022. "Prediction of Recoater Crash in Laser Powder bed Fusion Additive Manufacturing Using Graph Theory Thermomechanical Modeling." *Progress in Additive Manufacturing*, doi:10.1007/s40964-022-00331-5.
- Kumar, G. R., M. Sathishkumar, M. Vignesh, M. Manikandan, G. Rajyalakshmi, R. Ramanujam, and N. Arivazhagan. 2022. "Metal Additive Manufacturing of Commercial Aerospace Components – A Comprehensive Review, Proceedings of the Institution of Mechanical Engineers." *Part E: Journal of Process Mechanical Engineering* 441–454. doi:10.1177/09544089221104070.
- Land, W. S., B. Zhang, J. Ziegert, and A. Davies. 2015. "In-Situ Metrology System for Laser Powder Bed Fusion Additive Process." *Procedia Manufacturing* 1: 393–403. doi:10.1016/j.promfg.2015.09.047.
- Li, Z., X. Liu, S. Wen, P. He, K. Zhong, Q. Wei, Y. Shi, and S. Liu. 2018. "In Situ 3D Monitoring of Geometric Signatures in the Powder-Bed-Fusion Additive Manufacturing Process via Vision Sensing Methods." *Sensors* 18 (4): 1180. <https://www.mdpi.com/1424-8220/18/4/1180> doi:10.3390/s18041180
- Li, E., Z. Zhou, L. Wang, R. Zou, and A. Yu. 2022. "Numerical Studies of Melt Pool and gas Bubble Dynamics in Laser Powder Bed Fusion Process." *Additive Manufacturing* 56: 102913. doi:10.1016/j.addma.2022.102913.
- Liu, J., and P. Wen. 2022. "Metal Vaporization and Its Influence During Laser Powder Bed Fusion Process." *Materials & Design* 215: 110505. doi:10.1016/j.matdes.2022.110505.
- Mahmoud, D., M. Magolon, J. Boer, M. A. Elbestawi, and M. G. Mohammadi. 2021. "Applications of Machine Learning in Process Monitoring and Controls of L-PBF Additive Manufacturing: A Review." *Applied Sciences* 11 (24): 11910. <https://www.mdpi.com/2076-3417/11/24/11910> doi:10.3390/app112411910
- Mani, M., B. M. Lane, M. A. Donmez, S. C. Feng, and S. P. Moylan. 2017. "A Review on Measurement Science Needs for Real-Time Control of Additive Manufacturing Metal Powder bed Fusion Processes." *International Journal of Production Research* 55 (5): 1400–1418. doi:10.1080/00207543.2016.1223378.
- Meng, L., B. McWilliams, W. Jarosinski, H.-Y. Park, Y.-G. Jung, J. Lee, and J. Zhang. 2020. "Machine Learning in Additive Manufacturing: A Review." *JOM Journal of the Minerals Metals and Materials Society* 72 (6): 2363–2377. doi:10.1007/s11837-020-04155-y.
- Montazeri, M., A. R. Nassar, A. J. Dunbar, and P. Rao. 2020. "In-process Monitoring of Porosity in Additive Manufacturing Using Optical Emission Spectroscopy." *IIE Transactions* 52 (5): 500–515. doi:10.1080/24725854.2019.1659525.
- Montazeri, M., and P. Rao. 2018. "Sensor-Based Build Condition Monitoring in Laser Powder Bed Fusion Additive Manufacturing Process Using a Spectral Graph Theoretic Approach." *Journal of Manufacturing Science and Engineering* 140 (9): 091002. doi:10.1115/1.4040264.
- Montazeri, M., R. Yavari, P. Rao, and P. Boulware. 2018. "In-Process Monitoring of Material Cross-Contamination Defects in Laser Powder Bed Fusion." *Journal of Manufacturing Science and Engineering* 140 (11): 111001. doi:10.1115/1.4040543.
- Mostafaei, A., C. Zhao, Y. He, S. Reza Ghiaasiaan, B. Shi, S. Shao, N. Shamsaei, et al. 2022. "Defects and Anomalies in Powder bed Fusion Metal Additive Manufacturing." *Current Opinion in Solid State and Materials Science* 26 (2): 100974. doi:10.1016/j.cossms.2021.100974.
- Nassar, A. R., M. A. Gundermann, E. W. Reutzel, P. Guerrier, M. H. Krane, and M. J. Weldon. 2019. "Formation Processes for Large Ejecta and Interactions with Melt Pool Formation in Powder bed Fusion Additive Manufacturing." *Scientific Reports* 9 (1): 5038. doi:10.1038/s41598-019-41415-7.
- Nguyen, N. V., A. J. W. Hum, T. Do, and T. Tran. 2023. "Semi-supervised Machine Learning of Optical in-Situ Monitoring Data for Anomaly Detection in Laser Powder bed Fusion." *Virtual and Physical Prototyping* 18 (1): e2129396. doi:10.1080/17452759.2022.2129396.
- O. Additive. 2021. *AMSENSE-Advanced Quality Control for Metal Laser Powder Bed Fusion*. Accessed February 17, 2023. <https://openadditive.com/#amsense>.
- Okaro, I. A., S. Jayasinghe, C. Sutcliffe, K. Black, P. Paoletti, and P. L. Green. 2019. "Automatic Fault Detection for Laser Powder-bed Fusion Using Semi-Supervised Machine Learning." *Additive Manufacturing* 27: 42–53. doi:10.1016/j.addma.2019.01.006.
- Pandiyan, V., R. Drissi-Daoudi, S. Shevchik, G. Masinelli, T. Le-Quang, R. Logé, and K. Wasmer. 2021. "Semi-supervised Monitoring of Laser Powder bed Fusion Process Based on Acoustic Emissions." *Virtual and Physical Prototyping* 16 (4): 481–497. doi:10.1080/17452759.2021.1966166.
- Petrich, J., Z. Snow, D. Corbin, and E. W. Reutzel. 2021. "Multimodal Sensor Fusion with Machine Learning for Data-Driven Process Monitoring for Additive Manufacturing." *Additive Manufacturing* 48: 102364. doi:10.1016/j.addma.2021.102364.
- Polonsky, A. T., and T. M. Pollock. 2020. "Closing the Science Gap in 3D Metal Printing." *Science* 368 (6491): 583–584. doi:10.1126/science.abb4938. <https://www.science.org/doi/abs/10.1126science.abb4938>.
- Ramirez, B. S., and J. G. Ramirez. 2018. *Douglas Montgomery's Introduction to Statistical Quality Control: A JMP Companion*. Cary, NC: Sas Institute.
- Sames, W. J., F. A. List, S. Pannala, R. R. Dehoff, and S. S. Babu. 2016. "The Metallurgy and Processing Science of Metal Additive Manufacturing." *International Materials Reviews* 61 (5): 315–360. doi:10.1080/09506608.2015.1116649.
- Sanchez, S., P. Smith, Z. Xu, G. Gaspard, C. J. Hyde, W. W. Wits, I. A. Ashcroft, H. Chen, and A. T. Clare. 2021. "Powder Bed Fusion of Nickel-Based Superalloys: A Review." *International Journal of Machine Tools and Manufacture* 165: 103729. doi:10.1016/j.ijmactools.2021.103729.
- Schwerz, C., and L. Nyborg. 2021. "Linking In Situ Melt Pool Monitoring to Melt Pool Size Distributions and Internal Flaws in Laser Powder Bed Fusion." *Metals* 11 (11): 1856. doi:10.3390/met11111856. <https://www.mdpi.com/2075-4701/11/11/1856>.
- Scime, L., and J. Beuth. 2018a. "Anomaly Detection and Classification in a Laser Powder bed Additive Manufacturing Process Using a Trained Computer Vision Algorithm." *Additive Manufacturing* 19: 114–126. doi:10.1016/j.addma.2017.11.009.

- Scime, L., and J. Beuth. 2018b. "A Multi-Scale Convolutional Neural Network for Autonomous Anomaly Detection and Classification in a Laser Powder bed Fusion Additive Manufacturing Process." *Additive Manufacturing* 24: 273–286. doi:10.1016/j.addma.2018.09.034.
- Scime, L., and J. Beuth. 2019. "Using Machine Learning to Identify in-Situ Melt Pool Signatures Indicative of Flaw Formation in a Laser Powder bed Fusion Additive Manufacturing Process." *Additive Manufacturing* 25: 151–165. doi:10.1016/j.addma.2018.11.010.
- Shi, L. 2007. "Bounds on the (Laplacian) Spectral Radius of Graphs." *Linear Algebra and its Applications* 422 (2): 755–770. doi:10.1016/j.laa.2006.12.003.
- Smoqi, Z., A. Gaikwad, B. Bevans, M. H. Kobir, J. Craig, A. Abul-Haj, A. Peralta, and P. Rao. 2022. "Monitoring and Prediction of Porosity in Laser Powder bed Fusion Using Physics-Informed Meltpool Signatures and Machine Learning." *Journal of Materials Processing Technology* 304: 117550. doi:10.1016/j.jmatprotec.2022.117550.
- Snow, Z., A. R. Nassar, and E. W. Reutzel. 2020. "Invited Review Article: Review of the Formation and Impact of Flaws in Powder bed Fusion Additive Manufacturing." *Additive Manufacturing* 36: 101457. doi:10.1016/j.addma.2020.101457.
- Spears, T. G., and S. A. Gold. 2016. "In-process Sensing in Selective Laser Melting (SLM) Additive Manufacturing." *Integrating Materials and Manufacturing Innovation* 5 (1): 16–40. doi:10.1186/s40192-016-0045-4.
- Takezawa, A., Q. Chen, and A. C. To. 2021. "Optimally Variable Density Lattice to Reduce Warping Thermal Distortion of Laser Powder bed Fusion." *Additive Manufacturing* 48: 102422. doi:10.1016/j.addma.2021.102422.
- Tootooni, M. S., P. K. Rao, C. A. Chou, and Z. J. Kong. 2018. "A Spectral Graph Theoretic Approach for Monitoring Multivariate Time Series Data from Complex Dynamical Processes." *IEEE Transactions on Automation Science and Engineering* 15 (1): 127–144. doi:10.1109/TASE.2016.2598094.
- Ulbricht, A., G. Mohr, S. J. Altenburg, S. Oster, C. Maierhofer, and G. Bruno. 2021. "Can Potential Defects in LPBF Be Healed from the Laser Exposure of Subsequent Layers? A Quantitative Study." *Metals* 11 (7): 1012. doi:10.3390/met11071012.
- Wang, C., X. P. Tan, S. B. Tor, and C. S. Lim. 2020. "Machine Learning in Additive Manufacturing: State-of-the-art and Perspectives." *Additive Manufacturing* 36: 101538. doi:10.1016/j.addma.2020.101538.
- Wirth, F., A. Frauchiger, K. Gutknecht, and M. Cloots. 2021. "Influence of the Inert Gas Flow on the Laser Powder Bed Fusion (LPBF) Process." In *Industrializing Additive Manufacturing*, edited by M. Meboldt, and C. Klahn, 192–204. Cham: Springer International Publishing. doi:10.1007/978-3-030-54334-1\_14
- Xiao, L., M. Lu, and H. Huang. 2020. "Detection of Powder bed Defects in Selective Laser Sintering Using Convolutional Neural Network." *The International Journal of Advanced Manufacturing Technology* 107 (5): 2485–2496. doi:10.1007/s00170-020-05205-0.
- Yakout, M., and M. A. Elbestawi. 2020. "Residual Stress Formation in Laser-Based Powder Bed Fusion (PBF-LB) of Invar 36." In *Structural Integrity of Additive Manufactured Materials and Parts*, edited by N. Shamsaei, and M. Seifi, 34–44. West Conshohocken, PA: ASTM International. doi:10.1520/STP163120190149
- Yakout, M., I. Phillips, M. A. Elbestawi, and Q. Fang. 2021. "In-situ Monitoring and Detection of Spatter Agglomeration and Delamination During Laser-Based Powder bed Fusion of Invar 36." *Optics & Laser Technology* 136: 106741. doi:10.1016/j.optlastec.2020.106741.
- Yavari, R., A. Riensche, E. Tekerek, L. Jacquemetton, H. Halliday, M. Vandever, A. Tenequer, et al. 2021a. "Digitally Twinned Additive Manufacturing: Detecting Flaws in Laser Powder bed Fusion by Combining Thermal Simulations with in-Situ Meltpool Sensor Data." *Materials & Design* 211: 110167. doi:10.1016/j.matdes.2021.110167.
- Yavari, R., Z. Smoqi, A. Riensche, B. Bevans, H. Kobir, H. Mendoza, H. Song, K. Cole, and P. Rao. 2021b. "Part-scale Thermal Simulation of Laser Powder bed Fusion Using Graph Theory: Effect of Thermal History on Porosity, Microstructure Evolution, and Recoater Crash." *Materials & Design* 204: 109685. doi:10.1016/j.matdes.2021.109685.